

Genetic architecture of inter-specific and -generic grass hybrids by network analysis on multi-omics data

Elesandro Bornhofen^{1,*}, Dario Fè², Istvan Nagy³, Ingo Lenk², Morten Greve², Thomas Didion², Christian Sig Jensen², Torben Asp³, and Luc Janss^{1,*}

¹Center for Quantitative Genetics and Genomics, Aarhus University, Aarhus, Denmark

²Research Division, DLF Seeds A/S, Store Heddinge, Denmark

³Center for Quantitative Genetics and Genomics, Aarhus University, Slagelse, Denmark

*Corresponding authors: bornhofen@qgg.au.dk & luc.janss@qgg.au.dk

1 Abstract

2 Understanding the mechanisms underlining forage production and its biomass nutritive quality at the omics level is
3 crucial for boosting the output of high-quality dry matter per unit of land. Despite the advent of multiple omics inte-
4 gration for the study of biological systems in major crops, investigations on forage species are still scarce. Therefore,
5 this study aimed to combine multi-omics from grass hybrids by prioritizing omic features based on the reconstruction
6 of interacting networks and assessing their relevance in explaining economically important phenotypes. Transcrip-
7 toomic and NMR-based metabolomic data were used for sparse estimation via the fused graphical lasso, followed by
8 modularity-based gene expression and metabolite-metabolite network reconstruction, node hub identification, omic-
9 phenotype association via pairwise fitting of a multivariate genomic model, and machine learning-based prediction
10 study. Analyses were jointly performed across two data sets composed of family pools of hybrid ryegrass (*Lolium*
11 *perenne* × *L. multiflorum*) and *Festulolium loliaceum* (*L. perenne* × *Festuca pratensis*), whose phenotypes were
12 recorded for eight traits in field trials across two European countries in 2020/21. Our results suggest substantial
13 changes in gene co-expression and metabolite-metabolite network topologies as a result of genetic perturbation by
14 hybridizing *L. perenne* with another species within the genus relative to across genera. However, conserved hub genes
15 and hub metabolomic features were detected between pedigree classes, some of which were highly heritable and dis-
16 played one or more significant edges with agronomic traits in a weighted omics-phenotype network. In spite of tagging
17 relevant biological molecules as, for example, the light-induced rice 1 (*LIR1*), hub features were not necessarily better
18 explanatory variables for omics-assisted prediction than features stochastically sampled. The use of the graphical
19 lasso method for network reconstruction and identification of biological targets is discussed with an emphasis on
20 forage grass breeding.

21 **Keywords:** Graphical lasso, metabolome, multi-trait mixed model, network science, polyploid, transcriptome.

22 Background

23 Forage grasses cover large portions of agricultural land worldwide, efficiently converting enormous amounts of
24 natural resources into macronutrients used primarily for feed. Their relevance can be recognized by the extent
25 of the network of researchers and breeding organizations devoted to maximizing production efficiency. This

Abbreviations: ADF, acid detergent fiber; ADL, acid deterged lignin; BIC, Bayesian information criterion; BLUE, best
linear unbiased estimator; DMDig, dry matter digestibility; DMY, dry matter yield; FDR, false discovery rate; FL, *Festulolium*
loliaceum; GBS, genotyping-by-sequence; GO, gene ontology; GRM, genomic relationship matrix; HR, hybrid ryegrass; IQR,
interquartile range; JGL, joint graphical lasso; LRT, log-likelihood ratio test; MAF, minor allele frequency; NDF, neutral
deterged fiber; NDfd, digestible NDF; NIR, near-infrared spectroscopy; NMR, nuclear magnetic resonance; OOB, out-of-the-
bag accuracy; PC, principal component; Prot, protein; REML, restricted maximum likelihood; RNA-seq, RNA sequencing; SNP,
single nucleotide polymorphism; WSC, water-soluble carbohydrate.

26 has been largely achieved by conventional breeding techniques aiming to explore genetic variation not only
27 within but also across species and genera over the last decades. As biotechnology surged, breeders advanced
28 in experimenting with hybridizations across species and genera, leading to the release of successful varieties
29 of polyploid hybrid ryegrass (*L. perenne* × *L. multiflorum*) and *Festulolium loliaceum* (*L. perenne* × *F. pratensis*), for example. As high-throughput sequencing platforms reduced genotyping costs, genomics began to play a significant role across grass breeding programs, reshaping breeding pipelines aiming at the optimization of resource allocation mainly via genome-wide selection (Keep et al. 2020; Arojju et al. 2020; Fè et al. 2015). Recently, the complex problem of predicting phenotypes and finding candidate biological molecules associated with it can also be supported not only by marker information at the DNA level but also via transcriptomics (Pignon et al. 2021) and metabolomics (Wen et al. 2014), leading to a holistic view of the phenomena controlling the expression of economically important traits.

37 Improving existing weaknesses of elite genetic materials or simply unlocking genetic variability for breeding
38 exploitation are processes that benefited by leveraging hybridization across genera and species within a genus.
39 In spite of being predominantly diploid ($2n = 2x = 14$), *L. perenne*, *L. multiflorum*, and *F. pratensis* can also be found as or induced to tetraploid states, which is essential for amphidiploid production. However, genomic instability is often reported and a shift to the ryegrass genome over generations can happen in crosses with fescues (Kopecký et al. 2017; Akiyama et al. 2012). Additionally, homeolog expression bias and expression level dominance can be observed in such allopolyploids (Glombik et al. 2021). Collectively, these phenomena may lead to distinct interactomes when hybridizations are performed across species, which can be analyzed through network reconstruction by leveraging high throughput omics data and appropriate statistical methods. Using RNA-seq data, (Hu et al. 2017) reported network topologies of allopolyploid cotton resembling more to one of the diploid species representing a progenitor besides a substantial domestication impact on the coexpression. Additional studies on expression modifications in allopolyploids remain scarce.

49 Adding extra layers of biological information also means increasing data dimensionality ($n \ll p$ problem). Reliable inferences in high dimensions require specific statistical procedures and an in-depth understanding of the underlining phenomena. Among the methods proposed for the analysis of high dimensional omics data (Bersanelli et al. 2016), the reconstruction and analysis of regulatory networks offer the possibility to prioritize omic features (Naserkheil et al. 2022), significantly reducing the searching space for downstream analyses. Organizing omic features in interacting networks can be seen as an approximation of the true existent interconnected biological system that reads the information encoded on the genome and ends with a functional organism. Reconstructed networks hold biological meaningful topological properties, for example, the presence of modules that might cluster nodes (omic features) performing specific biological functions (Li et al. 2015) and the existence of highly connected nodes. These hub nodes arise as biological networks are assumed to be scale-free, meaning that node degrees are power-law distributed (Pereira-Leal et al. 2004) and, therefore, few highly connected nodes are expected. The presence of these disproportionately connected hub nodes is an important topological property of networks as it may represent key genes/metabolites associated with biological pathways. Thus, it would be of special interest to investigate the extent to which hub omic features can be significantly linked to biomass yield and other economically important phenotypes of fodder grasses. Researchers have found hub genes affecting biomass accumulation in other families of plants, for example, in *Ulmus pumila* L. (Chen et al. 2021) and *Arabidopsis thaliana* (Liu et al. 2021). That being stated, one needs to first estimate the network to be able to explore its topological properties and this can be accomplished by leveraging graph theory and probability for modeling and representation of complex biological problems as probabilistic graphical models (Li et al. 2015).

69 Omics data as a graphical model is based on the estimation of conditionally independent relationships across
70 random variables in a multivariate setting. Learning a graphic in high-dimension requires dealing with a
71 situation where the number of unknown parameters exceeds the sample size. In this case, ℓ_1 -penalization has
72 been one of the main techniques used to make sparse inference in a Gaussian Markov random field (Friedman
73 et al. 2007), yielding a sparse structured precision matrix \sum^{-1} which, in turn, can be converted into an
74 undirected network and further analyzed for its topological properties. This approach has been applied to
75 the study of gene expression (Shahdoust et al. 2019; Wu et al. 2013) and metabolomic (Liu et al. 2022)

76 data in humans, with few examples in plants (Li and Jackson 2015; Kapoor et al. 2021; e Lima et al.
77 2018; Bartzis et al. 2017). With a selected set of candidate features recovered from gene co-expression and
78 metabolic networks, one can perform omic-phenotype integration. The simple correlation-based integration
79 method of omic variables and phenotypes is widely used, with examples in maize (Zhang et al. 2019) and for
80 the forage species *E. sibiricus* (Zheng et al. 2022). However, more robust approaches based on multivariate
81 multi-level models have also been applied (de Steenhuijsen et al. 2016; Nantongo et al. 2021), showing better
82 properties (Bo et al. 2014). Finding significant associations of genes and metabolites with dry matter yield
83 and nutritive quality traits in fodder grasses could reveal potential targets for quantitative trait dissection
84 studies, improve the omics-assisted selection of elite families, and shed light on regulatory processes of key
85 traits. Additionally, given the fact that a large part of the above-ground biomass is harvested in forage grasses,
86 it can be hypothesized that randomly sampled hub features are more likely to be linked to a phenotype of
87 interest compared to, for example, grain crops.

88 The inherent properties of an organism's interactome, especially the power-law distribution of interactions,
89 give plasticity in face of random disturbances. However, interferences on hub nodes may lead to severe product
90 alterations (Crombach and Hogeweg 2008), making them targets for genetic studies. Additionally, hub genes
91 appear to be associated with a variety of biological processes (Tahmasebi et al. 2019; Hollender et al. 2014;
92 Zheng et al. 2022; Hu et al. 2017) and had been mentioned as potential targets for the molecular breeding of
93 forage species (Yan et al. 2022). In the present study, we consider the problem of reconstructing the interplay
94 among biomolecules and narrowing down high-dimensional omics data to fewer hub features to further test
95 their association with quantitative traits evaluated in family pools of allopolyploid grasses. Furthermore,
96 having significantly associated hubs would confirm the relevance of these interacting biomolecules, which
97 could be targeted for molecular biology studies and marker-assisted breeding. Our objective is, therefore,
98 to prioritize omic features in forage grasses by sparse estimation via undirected graphical models, filter the
99 relevant ones, and expand on their biological functions for biomass accumulation.

100 Methods

101 Plant material and phenotypes

102 Interspecific hybridization of *L. perenne* × *L. multiflorum* (hybrid ryegrass) and intergeneric crosses of *L.*
103 *perenne* × *F. pratensis* (*Festulolium loliaceum*), all in tetraploid forms ($2n = 4x = 28$), were performed as
104 two connected (by *L. perenne* parents) sparse dialles in the summer of 2017 at the DLF Seeds A/S research
105 station, Store Heddinge - Denmark. Single plants used as parents were extracted from commercial varieties
106 of *L. perenne*, *L. multiflorum*, and *F. pratensis*. A total of 79 and 65 allotetraploid families of hybrid ryegrass
107 and *Festulolium loliaceum*, respectively, were obtained out of several attempts. Hybrid ryegrass (referred to
108 hereinafter as HR) families were obtained after crossing 31 *L. perenne* parents with 79 *L. multiflorum* in a
109 sparse diallel design. For the pedigree class *F. loliaceum* (referred to hereinafter as FL), 24 *L. perenne* pa-
110 rents out of the 31 from the HR diallel were crossed with four *F. pratensis* parents. A sufficient quantity of
111 seeds of F_3 families was obtained after two rounds of multiplication. The field trials were carried out in the
112 autumn of 2020 at two testing sites: i) Denmark ($55^{\circ} 17' 52''$ N, $12^{\circ} 24' 58''$ E) and ii) the Czech Republic
113 ($49^{\circ} 40' 59''$ N, $17^{\circ} 58' 05''$ E). Families from the HR pedigree class were sown in Denmark in plots of 12.5
114 m^2 with two replicates while families of the FL pedigree class were sown in the Czech Republic in plots of 6.25
115 m^2 , also with two replicates. At each location, entries were assigned to plots arranged in five smaller trials
116 in a randomized complete block design with ~ 16 entries each. Alongside the described steps, seeds from F_2
117 families were sown in a greenhouse environment in 2019 at Aarhus University, Research Center Flakkebjerg.
118 One gram of seeds from each family was sown in pots 10 cm in diameter aiming at 120 to 150 emerging
119 individual plants. The total above-ground biomass was harvested as one bulk per family, flash-frozen using
120 liquid nitrogen to stop metabolism, and placed in a -80°C freezer. Frozen tissue ground into a fine powder
121 with liquid nitrogen was used for RNA isolation and sequencing after a quality check. In addition, aliquots
122 weighing 300 mg from ground tissue were freeze-dried for NMR-based metabolomic profiling.

123 We collected phenotypes for eight traits at four-time points in Denmark and three-time points in the Czech

124 Republic across the Spring, Summer, and Autumn of the 2021 production year. The following traits were
125 assessed: moisture-corrected dry matter yield standardized by plot size (DMY, g m⁻²), acid-detergent fiber
126 (ADF), acid-deterged lignin (ADL), dry matter digestibility (DMDig), neutral deterged fiber (NDF), diges-
127 tible NDF (NDFD), protein (Prot), and water-soluble carbohydrates (WSC). All nutritive quality traits are
128 expressed as a percentage of DMY, except for NDFD, which is a percentage of NDF. Nutritive quality traits
129 were obtained via a near-infrared (NIR) spectrometer onboard the plot combine harvester. Raw NIR data
130 had previously been calibrated and is yearly updated with new wet chemistry analysis, a routine procedure
131 in the breeding company.

132 Multi-omics data

133 Gene expression via RNA sequencing

134 RNASeq libraries were prepared and sequenced at the Beijing Genomics Institute (BGI Hong Kong) using
135 the BGISEQ-500RS sequencing platform technology in 100nt paired-end (PE100) mode. Paired-end reads
136 (20 to 25M sequences per sample) were mapped to pseudo-chromosomes and scaffolds of the *Lolium*.2.6.1
137 reference genome ([Nagy et al. 2022](#)) using the splice-aware aligner HISAT2 ([Kim et al. 2019](#)). Alignments were
138 processed by StringTie ([Pertea et al. 2015](#)) for transcript reconstruction and gene expression quantification.
139 Normalized read count values in fragments per kilobase of transcript per million (FPKM) were collected for
140 139,004 transcripts annotated on the *Lolium*.2.6.1 reference genome. A filter was applied to the expression
141 profile matrix to get rid of transcripts with expression values very low/equal to zero. The threshold for
142 transcription was set to 0.5 median FPKM across all samples, yielding the final filtered gene expression
143 matrix with 18,499 transcripts.

144 RNASeq-based genetic variants

145 Variant calling was performed from RNA-seq merged BAM-format alignments using the Bayesian genetic
146 variant detector Freebayes ([Garrison and Marth 2012](#)). The initial single-nucleotide polymorphism (SNP)
147 calling resulted in 1,689,206 variants. After retaining only biallelic markers, we filtered variants by the
148 following criteria: i) a maximum missing proportion of 50% at each locus, ii) a minimum mapping quality
149 of 20, iii) a minimum read coverage of five reads per variant position, and iv) minor allele frequency (MAF)
150 greater than 0.05. The final set of SNPs comprises 89,862 variants that were used for downstream analyses.

151 NMR-based metabolomic data

152 The metabolomic profiling by proton nuclear magnetic resonance spectroscopy (1H-NMR) was carried out at
153 the Natural Products Laboratory (The Netherlands). Following the sample preparation and spectra acquisi-
154 tion with a 600 MHz Bruker AVANCE III spectrometer (Bruker BioSpin GmbH, Germany), the raw NMR
155 data were processed using the software package NMRProcFlow ([Jacob et al. 2017](#)). After chemical shift cal-
156ibration and normalization, metabolomic fingerprinting yielded a total of 556 bins with non-zero intensities
157 (referred to hereafter as NMR variables) for 144 plant samples by applying an adaptive Intelligent Binning
158 [AI-Binning, ([Meyer et al. 2008](#))] algorithm. A tab-separated file with samples on rows, NMR variables on
159 columns, and cell-wise intensity values was generated for downstream analysis.

160 Statistical analysis

161 Prior exploratory analysis revealed considerable differences between the omics data from the HR class com-
162 pared to FL class samples. Therefore, downstream analyses were performed considering each of the two
163 classes as distinct but related across layers of omics data. Additionally, this decision was supported by the
164 fact that phenotypes were assessed in different locations, lacking connectedness. Later, these data sets were
165 merged for an omic-assisted prediction study.

166 Allele frequency-based genomic kernel

167 The genomic relationship matrix (GRM), which gives the realized genetic similarities among any pair of
168 individuals, was computed for SNP data sets of sizes $p \times n$ equal to $85,283 \times 79$ for the HR and $75,299 \times 65$
169 for FL data sets after individually re-filtering by MAF, depth, and missing rate using the same thresholds
170 as described before. The GRM was then used for downstream omics feature corrections due to popula-
171 tion stratification and multivariate mixed model analysis. The GRM based on pooled DNA was calculated

172 using (VanRaden 2008) method 2 adapted to use allele frequencies instead of discrete genotype calls. First, a
 173 column-centered matrix \mathbf{M} was computed as $\mathbf{M} = \{\mathbf{f}_j - \bar{\mathbf{f}}_j\}$, with j indexing SNP markers, \mathbf{f}_j representing a
 174 vector of alternative allele frequencies for SNP j , and $\{\dots\}$ represents a matrix built up with column vectors.
 175 The matrix \mathbf{G} can then be obtained as shown in Eq. 1.

$$\mathbf{G} = \frac{\mathbf{M}\mathbf{M}'}{\frac{1}{n} \sum_{i=1}^m \hat{p}_j (1 - \hat{p}_j)} \quad (1)$$

176 where n is the ploidy of the breeding material, m is the number of markers, and \hat{p}_j represents the frequency
 177 at j th locus simply obtained by taking the column means of the \mathbf{M} matrix. As outbred full-sib F_2 families of
 178 tetraploid plants, the genotype of a family can be described as octoploid (Ashraf et al. 2014). Therefore, the
 179 realized relatedness is obtained by scaling the plain genomic relationship matrix from the cross product of \mathbf{M}
 180 by the expected SNP variances, yielding a kernel that is analogous to the traditional numerator relationship
 181 matrix, also known as the \mathbf{A} matrix. Finally, a diagonal correction was applied to \mathbf{G} considering ploidy
 182 number and coverage depth as proposed by (Cericola et al. 2018).

183 Adjustment for population stratification

184 The impute file for the analysis of gene expression data consisted of two subsets of 4,767 features times
 185 the number of samples of each pedigree class. The reduced set of genes was obtained after further filtering
 186 out transcripts with more than 50% of samples having zero reads and retaining positions with at least 10
 187 or more samples having 10 or more reads. Additionally, a filter on the expressional variance of non-zero
 188 elements was performed, selecting features ranked in the top 50th percentile as the variation for genes in the
 189 bottom may be largely due to non-biological noise. Finally, we retained only features common to both data
 190 sets followed by the addition of a pseudo count to the expression matrix, which was subsequently log(2)-
 191 transformed [$\log_2(x+1)$]. The input file for the analysis of NMR data consisted of two subsets of 556 NMR
 192 variables for each pedigree class. NMR features were mean-centered and variable intensities were addressed
 193 via Pareto scaling, which uses the square root of the standard deviation to reduce the relative importance
 194 of high-variance features across the spectrum without much disturbance to the data structure.

195 Population stratification was detected in an unsupervised manner via the multivariate statistical technique
 196 of principal component analysis and corrected via regression modeling. We empirically retained coordinates
 197 of the top 10 eigenvectors of each k pedigree class to regress out population stratification as well as possible
 198 batch effects among samples. Therefore, the transcriptomic and metabolomic data sets were feature-wise
 199 corrected by incorporating principal component scores in the linear model of the form described in Eq. 2.

$$y_i = \mu + \sum_{p=1}^P (x_{ip}^{PC} \beta_p) + \varepsilon_i \quad (2)$$

200 where, y_i represents the response variable i (omic feature); x_{ip}^{PC} is the entry-specific coordinates of the p th
 201 principal component, with $p = 1 \dots P$ where P is equal to 10, β_p is the fixed regression coefficients adjusting
 202 for population stratification, and ε_i is the residual which was retained to reconstruct the full corrected omics
 203 data sets for network estimation.

204 Joint graphical lasso analysis for inverse covariance estimation

205 A joint graphical lasso (JGL) method was used for estimation in a scenario of double-related Gaussian
 206 graphical models. The two-class problem of high dimensional features was present in the data set due to
 207 the available inter-species/genus crosses. One can expect similar graphical models between the two classes
 208 as parents were shared among crosses between them, but also some nuances once the involved species have
 209 substantial differences regarding phenotypic traits. Therefore, the joint graphical lasso proposed by (Danaher
 210 et al. 2014) can handle this situation by estimating two graphical models, one for each pedigree class,
 211 and borrowing information across classes. For each pedigree class k ($k = 1, 2$), let a data matrix $\mathbf{X}^{(k)}$
 212 represent column-centered data with p omic features, and $\mathbf{X}^{(k)} \sim N(\mu^{(k)}, \Sigma^{(k)})$, where $\Sigma^{(k)}$ is a positive

213 definite $p \times p$ covariance matrix of the omic features. The inverse of $\Sigma^{(k)}$ is the precision matrix $\Theta^{(k)}$
 214 representing the network structure of omic features. By applying an ℓ_1 -penalty on $\Theta^{(k)}$ the network is
 215 made sparse, where elements will be 0 for conditionally independent pairs of features given the remaining
 216 variables. The sparsity condition allows learning graphics even in small sample sizes. The fused graphical
 217 lasso formulation in which $\Theta^{(k)}$ are estimated by maximizing the penalized form of the likelihood function
 218 for the two classes is shown in Eq. 3.

$$\underset{\{\Theta\}}{\text{maximize}} \quad \left\{ \sum_{k=1}^2 n_k \left(\log \det \Theta^{(k)} - \text{trace} \left(\mathbf{S}^{(k)} \Theta^{(k)} \right) \right) - P(\{\Theta\}) \right\} \quad (3)$$

219 where $P(\{\Theta\})$ is as follows:

$$P(\{\Theta\}) = \lambda_1 \sum_{k=1}^2 \sum_{i \neq j} |\theta_{ij}^k| - \lambda_2 \sum_{h < k} \sum_{i,j} |\theta_{ij}^h - \theta_{ij}^k| \quad (4)$$

220 here, $\mathbf{S}^{(k)}$ is the empirical covariance matrix of omics features calculated as $\mathbf{S}^{(k)} = n^{-1} \mathbf{X}^{(k)} \mathbf{X}^{(k)T}$. The
 221 optimization problem is here solved by the alternating direction method of multipliers (ADMM) algorithm.
 222 The solution to the problem of $n \ll p$ in the joint graphical lasso model is based on a penalized log-likelihood
 223 approach. In addition, as can be seen in Eq. 4, running JGL requires tuning two nonnegative parameters (λ_1
 224 and λ_2). The λ_1 penalty controls the degree of sparsity while λ_2 determines network similarity. If λ_2 is zero
 225 (i.e., no penalty is imposed) then $\Theta^{(k)}$ are independent and no information is shared between them. To select
 226 the proper hyperparameters, we used a goodness-of-fit approach where a grid search was performed to select
 227 values that minimize the Bayesian information criterion [BIC] (Schwarz 1978) specified in Eq. 5 (Augugliaro
 228 et al. 2016), yielding values that balance model likelihood and complexity.

$$BIC(\lambda_1, \lambda_2) = \sum_{k=1}^2 \left[n_k \left\{ \text{tr}(\mathbf{S}^{(k)} \hat{\Theta}^{(k)}) - \log \det \hat{\Theta}^{(k)} \right\} + \log n_k \sum_{i \leq j} \mathbf{1}_{\{\hat{\Theta}_{ij}^k \neq 0\}} \right] \quad (5)$$

229 In order to reduce the computational burden, a dense search was performed over λ_1 for each fixed value
 230 of λ_2 and a quick search for the former parameter for each fixed value of λ_1 as suggested by (Danaher et
 231 al. 2014). For the metabolomic data set, a uniform log spaced grid starting from 0.01 to 20 with a size
 232 equal to 30 was defined for λ_1 whereas a simple sequence equally spaced from 0 to 0.5 (size of 15) was
 233 defined for λ_2 . The same grid search space was defined for transcriptomic data, however, smaller sizes of 15
 234 for λ_1 and 10 for λ_2 were specified. After selecting the proper hyperparameter values, we run JGL for each
 235 omics data set producing four precision matrices $\Theta^{(k)}$. From these matrices, one can compute the partial
 236 correlation between pairs of dependent features as $\text{corr}_{ij|V \setminus \{i,j\}} = -\theta_{ij} / \sqrt{\theta_{ii}\theta_{jj}}$. The joint graphical lasso
 237 method implemented in the R package JGL (Danaher et al. 2014) was used for network estimation.

238 **Network reconstruction, candidate modules, and hub identification**

239 Network analyses aiming for complexity reduction were performed in order to prioritize candidate genes and
 240 metabolomic features for further integration with phenotypes of interest. Initially, each precision matrix $\Theta^{(k)}$
 241 was converted into a symmetric (graph is undirected) 0-1 matrix of dimensions equal to $p \times p$, referred to as
 242 the adjacency matrix $\mathbf{A}^{(k)}$ for each k data set following the definition:

$$\mathbf{A}_{ij}^{(k)} = \begin{cases} 1 & \text{if } \Theta_{ij}^{(k)} \neq 0, i \neq j; \\ 0 & \text{otherwise} \end{cases} \quad (6)$$

243 Four adjacency matrices \mathbf{A} were obtained and from them, we created graphic objects using the R package
 244 `igraph` (Csardi and Nepusz 2006). Initially, a graph is denoted as $G = (V, E)$ in which each node $v \in V$
 245 represents a biomolecule in this study, whereas each edge $e = (v_i, v_j) \in E$ refers to the interaction between
 246 pairs of nodes v_i and v_j . Each graph was organized in modules (communities) via a multi-level modularity
 247 optimization algorithm (Blondel et al. 2008), forcing highly connected edges to cluster in modules that
 248 are sparsely connected among them. In other words, more edges occur within identified modules than the
 249 quantity expected at random. The community structure is essential for finding hub nodes that are more
 250 likely to be involved in different biological processes.

251 Hub features were identified intramodule via maximum Kleinberg's hub centrality score, which is the principal
 252 eigenvector of $\mathbf{A}^{(k)} \cdot (\mathbf{A}^{(k)})^T$ (Kleinberg 1999). By using the hub scores, one can identify the most influential
 253 features in the network and explore the biological function of these interacting biomolecules. Therefore, we
 254 selected the top five hub features per module and kept only those intersecting across data sets to maximize
 255 the probability of selecting true/conserved hubs of genes and metabolites.

256 **REML variance components and heritability**

257 Single omic features were analyzed by fitting a linear mixed model of the form: $\mathbf{y} = \mathbf{1}\mu + \mathbf{Z}\mathbf{u} + \mathbf{e}$, where \mathbf{y}
 258 is the response vector (normalized gene expression values or total area of the bin from the bucketed NMR
 259 spectrum), $\mathbf{1}$ is a vector of ones linking observations to the constant μ , $\mathbf{u} \sim N(\mathbf{0}, \mathbf{G}\sigma_u^2)$, and $\mathbf{e} \sim N(\mathbf{0}, \mathbf{I}\sigma_e^2)$ are
 260 vectors of the random additive genetic with covariance structure \mathbf{G} (Equation 1) and independent (identity
 261 matrix \mathbf{I} as covariance structure) residual effects, respectively. \mathbf{Z} is the design matrix assigning observations
 262 of omic features to the respective F_2 family. The genomic heritability was calculated as $h_g^2 = \sigma_u^2 / (\sigma_u^2 + \sigma_e^2)$,
 263 where h_g^2 measures the proportion of the variance attributed to allele substitution effects captured by the
 264 genomewide markers relative to the total variance.

265 Phenotypic variance within location was partitioned into the terms defined by the linear mixed model
 266 displayed in Equation 7:

$$\mathbf{y} = \mathbf{X}\beta + \mathbf{Z}\mathbf{u} + \sum_{i=1}^{11} \mathbf{S}_i \mathbf{s} + \mathbf{e} \quad (7)$$

267 where, \mathbf{y} , β , \mathbf{u} , \mathbf{s} , and \mathbf{e} represent the vectors of the response variable, fixed trial-block effect, random additive
 268 genetic effect following $\mathbf{u} \sim N(\mathbf{0}, \mathbf{G}\sigma_u^2)$, random spatial effect following $\mathbf{s} \sim N(\mathbf{0}, \mathbf{I}\sigma_s^2)$, and random residual
 269 effect assumed $\mathbf{e} \sim N(\mathbf{0}, \mathbf{I}\sigma_e^2)$, respectively. Matrices \mathbf{G} and \mathbf{I} are as defined before. Design matrices \mathbf{X} , \mathbf{Z} ,
 270 and \mathbf{S} link observations of the response variable to the specific model effect. The spatial effect is a sliding
 271 window accounting for 10 neighboring plots in addition to the target experimental unit and works by scanning
 272 the field for spatial variation not accounted for by the prior trial design. Genomic heritability was calculated
 273 as: $h_g^2 = \sigma_u^2 / (\sigma_u^2 + 11\sigma_s^2 + \sigma_e^2)$. Variance components and heritabilities for eight phenotypic traits can be
 274 found in the supplemental Table S1. Finally, the parameter σ_u^2 was multiplied by the average diagonal of the
 275 GRM in both heritability equations presented before.

276 **Phenotypes and omics integration via pairwise fitting of mixed models**

277 The raw phenotypic data were analyzed alongside hub omic features in a multitrait genome-wide fashion via
 278 linear mixed models to investigate pair-wise additive genetic correlations. The bivariate model (Eq. 8 and 9)
 279 was fitted lm times, combining l hub nodes and m phenotypic traits, for each data set, yielding correlations
 280 used to describe the existence of a significant association between the concentration of selected biological
 281 molecules and economically important phenotypes.

$$\mathbf{y}_{OME_l} = \mathbf{X}_1 \beta_{OME_l} + \mathbf{X}_2 \mathbf{b}_{OME_l} + \mathbf{Z} \mathbf{u}_{OME_l} + \mathbf{e}_{OME_l} \quad (8)$$

$$\mathbf{y}_{PHE_m} = \mathbf{X}_1 \beta_{PHE_m} + \mathbf{X}_2 \mathbf{b}_{PHE_m} + \mathbf{Z} \mathbf{u}_{PHE_m} + \sum_{i=1}^{11} \mathbf{S}_i \mathbf{s}_{PHE_m} + \mathbf{e}_{PHE_m} \quad (9)$$

282 where \mathbf{y}_{OME_l} and \mathbf{y}_{PHE_m} are vectors of expression/intensities of hub omic features and records of phenotypic traits, respectively; β_{OME_l} contains the fixed general mean effect while β_{PHE_m} also contains the fixed effect of block within trial; vectors \mathbf{b}_{OME_l} and \mathbf{b}_{PHE_m} contains fixed regression coefficients estimated by regressing response variables on principal components' dimensional scores calculated from the genomic kernel; \mathbf{u}_{OME_l} and \mathbf{u}_{PHE_m} are vectors of families' additive genetic effect; \mathbf{s}_{PHE_m} is the vector of random spatial effect with $\mathbf{s}_{PHE_m} \sim N(0, \mathbf{I}\sigma_{s_{PHE_m}}^2)$; and \mathbf{e}_{OME_l} and \mathbf{e}_{PHE_m} are vectors of random residuals for expression/intensity of hub omic feature l and phenotypic trait m , respectively. For incidence matrices \mathbf{X} linking fixed effects to response variables, the general mean was the only fixed effect for submodel 8, thus $\mathbf{X}_1 = \mathbf{1}$. Matrices \mathbf{X}_2 contain scores of the top three principal components computed from the \mathbf{G} matrix (Eq. 1) instead of 1's and 0's, aiming at further accounting for population structure to avoid false-positive associations. The selection of the appropriate number of PC's followed an empirical evaluation of the changes in response variables' heritabilities as they were added. The matrix \mathbf{Z} is the corresponding incidence matrix of additive family effects. Finally, the series of matrices \mathbf{S}_i link the random spatial effect to the surrounding plots and work as a sliding window (cross-shaped format) mapping the field for microenvironmental variations missed by the blocking design. The joint covariance structure of the remaining random terms was assumed as follows:

$$\begin{bmatrix} \mathbf{u}_{OME_l} \\ \mathbf{u}_{PHE_m} \end{bmatrix} \sim N \left(\mathbf{0}, \mathbf{G} \otimes \begin{bmatrix} \sigma_{u_{OME_l}}^2 & \sigma_{u_{OME_l} u_{PHE_m}} \\ \sigma_{u_{OME_l} u_{PHE_m}} & \sigma_{u_{PHE_m}}^2 \end{bmatrix} \right) \quad (10)$$

297 and

$$\begin{bmatrix} \mathbf{e}_{OME_l} \\ \mathbf{e}_{PHE_m} \end{bmatrix} \sim N \left(\mathbf{0}, \mathbf{I} \otimes \begin{bmatrix} \sigma_{e_{OME_l}}^2 & 0 \\ 0 & \sigma_{e_{PHE_m}}^2 \end{bmatrix} \right) \quad (11)$$

298 where \mathbf{I} represents an identity matrix and \otimes is the Kronecker product. Besides the scores of the first three
299 principal components, here \mathbf{G} also accounts for the whole-genomic relationship structure of the population.
300 Covariances between response vectors were set to non-existent for residual genetic and error random effects.

301 For hypothesis testing, we also ran a constrained version of the bivariate model, setting the additive genetic
302 covariance between submodels 8 and 9 (Eq. 10) to zero ($\sigma_{u_{OME_l} u_{PHE_m}} = \sigma_{e_{OME_l} e_{PHE_m}} = 0$). The significance
303 of the additive genetic correlations was tested by comparing the constrained and unconstrained models via
304 a one-tailed log-likelihood ratio test (LRT) with 0.5 degrees of freedom (Gilmour et al. 2015; Self and
305 Liang 1987). Multiple testing correction was performed for coefficients across traits within omic features
306 via Benjamini-Hochberg false discovery rate (FDR) (Benjamini and Hochberg 1995) procedure at alpha
307 equals 0.05 aiming to control for type I error.

308 The lm additive genetic correlations estimated by fitting the full bivariate model for each data set were
309 retained along with the p-values and FDR-based significant associations and used for constructing the
310 omics-phenotype weighted network graph. A visualization of the network was produced using the software
311 Cytoscape 3.9.1 (Shannon et al. 2003), weighing edges by the magnitude of the trait-omic associations.

312 Gene ontology enrichment analysis

313 Transcript protein sequences were subjected to local InterPro analysis using InterProScan v5.28-67.0 (Jones
314 et al. 2014). Predictive information concerning conserved protein domains, signal peptides, transmembrane
315 domains, and gene ontology (GO) data was acquired from 14 member databases of InterPro. Per transcript,
316 non-redundant GO information was collected from InterPro outputs using custom scripts. GO-term
317 enrichment analysis was carried out using the Python library GOATOOLS (Klopfenstein et al. 2018) by
318 intersecting the GO-term list of the full perennial ryegrass transcriptome, the GO-term subset of expressed
319 genes, and the GO-term lists of filtered transcript sets (study lists). Significant enrichment was declared via
320 Fisher Exact Test, corrected for false discovery rate (Benjamini and Hochberg 1995).

321 **Omics-assisted prediction**

322 Starting from the centered **M** matrix of SNP markers defined before, missing allele frequencies were imputed
323 by chained random forest. This method was selected after comparing the ability in predicting missing allele
324 frequencies against the weighted K-nearest neighbors (KNN) method via cross-validation. The imputations
325 were performed for each pedigree class separately using the R package missRanger (Mayer 2021). The miss-
326 Ranger function ran using the arguments *num.trees* equal to 100, *sample.fraction* equal to 0.1, *max.depth* of
327 6, and *extratrees* for the *splitrule* argument. The imputation was performed by looping over one chromosome
328 at a time within clusters of SNPs created by running a complete-linkage clustering algorithm with $k = 30$
329 as the desired number of groups.

330 We used the best linear unbiased estimator (BLUE) of entries as response variables in the prediction study.
331 The adjusted phenotypes were obtained by rearranging the terms and refitting the submodel in Eq. 9 with
332 families as a fixed effect and no PC scores were included. BLUEs within locations were mean-centered to
333 remove differential environmental effects followed by the merging of phenotypes and predictors from HR
334 and FL data sets. The unsupervised machine learning algorithm random forest was used as the engine
335 for the prediction study. Models were fitted using the 'ranger' R package (Wright and Ziegler 2017) with
336 the hyperparameters minimum node size and a number of randomly drawn candidate features set to five
337 and $\lfloor \sqrt{n} \rfloor$, respectively, where n is the number of variables. Therefore, the random forest model was fitted on
338 the combined data sets, setting the number of decision trees to 2,000. Training out-of-the-bag accuracy (OOB
339 accuracy) was reported as a performance metric. Finally, variable importance was computed via permutation.

340 Three prediction scenarios were studied. First, we selected a subset of SNPs tagging common hub genes
341 across data sets, the common hub genes, and the common hub NMR variables as three sets of regressors.
342 The second scenario consisted of stochastically sampling 20x sets of 30 genes (then SNPs within these genes)
343 and 32 NMR variables aiming to compare the prediction power contained in hub nodes with randomly
344 sampled features. In the last scenario, we used all common SNPs, genes, and NMR variables as regressors.
345 Besides comparing prediction accuracy with the previous scenarios, here we can assess a common prediction
346 task where the goal is to evaluate the closeness of predicted and observed values using all available predictor
347 variables.

348 **Statistical computing and data visualization**

349 Large-scale computations were performed in the GenomeDK high-performance computing facility located
350 at Aarhus University, Denmark. Mixed model analyses were fitted using DMU package version 6 (Madsen
351 and Jensen 2013). Modular network visualizations were produced using the R package NetBioV (Tripathi
352 et al. 2014) with the Fruchterman-Reingold layout algorithm to arrange nodes in each module. Finally,
353 miscellaneous plots were drawn employing the ggplot2 R package (Wickham 2016).

354

Results

355

Genetic similarity among family pools and omics heritability

356 We constructed a genomic relationship matrix (GRM) for the *L. perenne* \times *L. multiflorum* (hybrid ryegrass;
357 HR pedigree class) using 85,283 SNPs and a GRM for the intergeneric crosses of *L. perenne* \times *F. pratensis* (*Festulolium loliaceum*; FL pedigree class) using 75,299 SNPs (Figure 1 A and B, respectively).
358 The average genomic relationship was close to zero as expected due to the centering of allele frequencies
359 in both data sets (-0.0178 and -0.024 for hybrid ryegrass and *F. loliaceum*, respectively) but with substan-
360 tially more variation found in the FL data set (off-diagonal standard deviation equal to 0.21 compared to
361 0.15 in the HR class). In addition, GRM heatmaps are substantially populated with negative relationships,
362 meaning that many pairs of individuals were less related than the average genomic relationship. Also, the
363 GRMs revealed biparental combinations that substantially deviated from the expected offspring composition
364 of bi-parental crosses of single-plant parents, suggested by the presence of blocks of high genomic relation-
365 ships (>1.0) among families, especially for the FL data set (Figure 1B). For instance, the 4×4 block on the
366 top-left side of Figure 1B holds highly related families that share the same pollen receptor parent crossed
367

368 with different *F. pratensis* genotypes. As the diallel design was not accounted for, downstream analyses were
 369 performed controlling for population stratification due to replicated parents in the crossing scheme using
 370 principal component (PC) scores as covariates. The first 10 PCs of the GRM matrices explained a cumulative
 371 percentage of variation equal to 75% and 82% for HR and FL data sets, respectively. Additionally, adjusted
 372 means on the right-hand side of Figure 1 reveal blocks of families with similar trait-specific performance as
 373 they were hierarchically clustered by IBS-based measurement of relatedness.

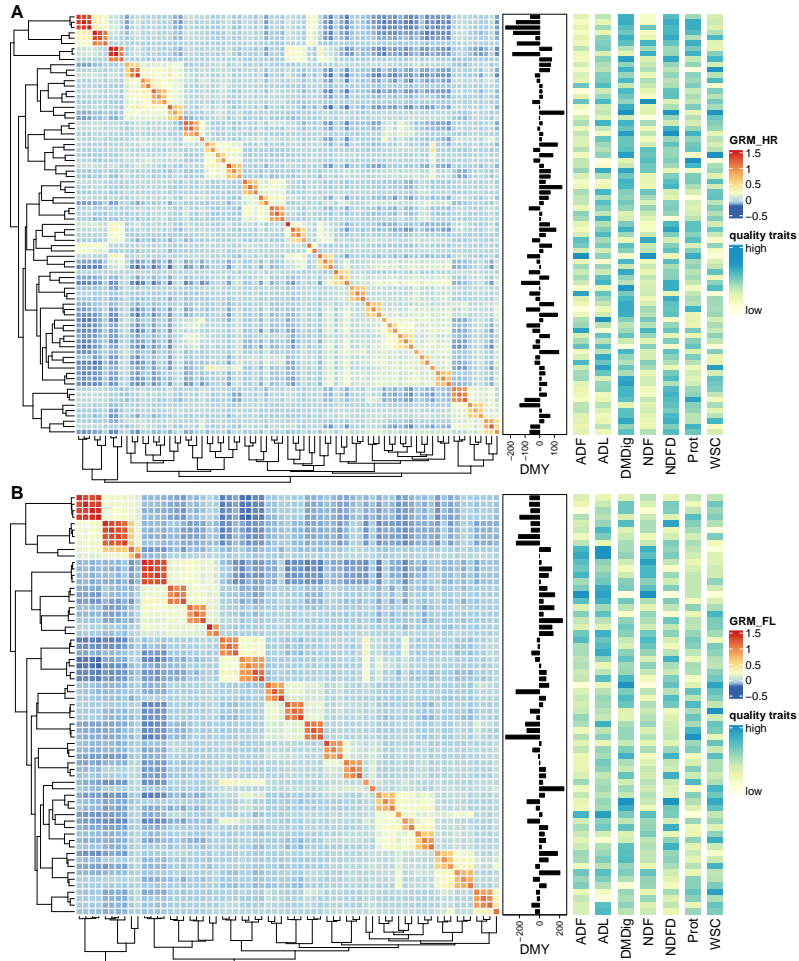


Figure 1: Allele frequency-based genomic relationship matrix (GRM) for 79 families of hybrid ryegrass [HR] (A) and 65 families of *Festulolium loliaceum* [FL] (B). Heatmap depictions of GRMs are annotated with best linear unbiased estimators (BLUEs) for dry matter yield (DMY) and each of the seven nutritive quality traits: ADF - acid detergent fiber; ADL - acid detergent lignin; DMDig - digestible dry matter; NDF: -neutral detergent fiber; NDFD - digestible NDF; Prot - protein; and WSC - water-soluble carbohydrates. Partially surrounding dendograms were produced using Euclidean as the distance measure and the agglomerative complete-linkage method to build the hierarchy of clusters.

374 The GRMs displayed in Figure 1 were also used in a linear mixed model to estimate the genomic heritability
 375 of NMR variables and gene expression entities. The density plots of the heritabilities for both pedigree classes
 376 are displayed in Figure 2. For the HR class, median heritabilities of 0.047 and 0.122 with an interquartile

377 range (IQR) of 0.177 and 0.311 were observed for NMR variables and gene expression, respectively. For
 378 the FL class, we observed median heritability of 0.162 and 0.165 with IQR of 0.273 and 0.295 for NMR
 379 variables and gene expression, respectively. Distributions are positively skewed and a higher quantity of high
 380 heritable variables can be detected for gene expression data in comparison to NMR variables. Additionally,
 381 the figure suggests a slightly higher proportion of more heritable features measured on samples from the FL
 382 class, especially for metabolomic data. Finally, subfigures 5B and 5C reveal the similarity in heritability
 383 between pedigree classes according to the spectrum and genomic position, respectively. Overall, there is a
 384 high correspondence between classes for regions displaying high and low heritability.

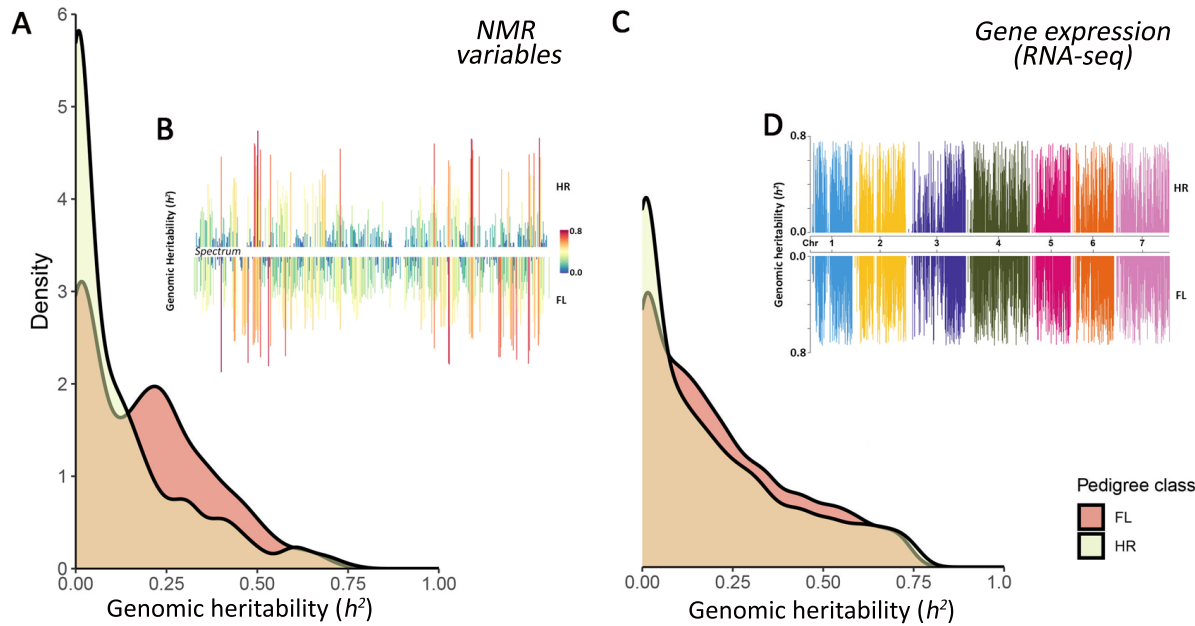


Figure 2: Density plots displaying the SNP-based genomic heritability distribution of NMR variables (A) and gene expression (C) from family pools of two pedigree classes (HR: hybrid ryegrass and FL: *Festulolium loliumaceum*). The genomic heritability of NMR variables is displayed along the spectrum for both pedigree classes in B and subfigure D displays the genomic heritability of gene expression data along genomic position across chromosomes also for both pedigree classes.

385 Hyperparameter tuning of joint graphical lasso

386 The search for the appropriate values of λ_1 and λ_2 that returned the smallest Bayesian information criterion
 387 (BIC) was computationally intensive as the model was fitted for all combinations of the penalties defined in
 388 the grid search, requiring several days of CPU time for joint graphical lasso (JGL) model of transcriptomic
 389 data but only using few wall time hours by taking advantage of multi-core processing. A total of 939
 390 connected nodes were estimated for gene expression. Within data sets, four sparse subnetworks and 4,038
 391 edges were obtained for HR whereas five sparse subnetworks and 2,182 edges were identified for the FL class
 392 given the tuning parameters selected via BIC (Figure 3). Additionally, 462 edges were found to be shared
 393 by the two pedigree crossing classes. For the next omic layer, all 556 nodes (NMR variables) were connected,
 394 one sparse network on each pedigree class was estimated, 7,757 and 4,789 edges were available for HR and
 395 FL data sets, respectively, and 2,371 common interactions shared by all classes.

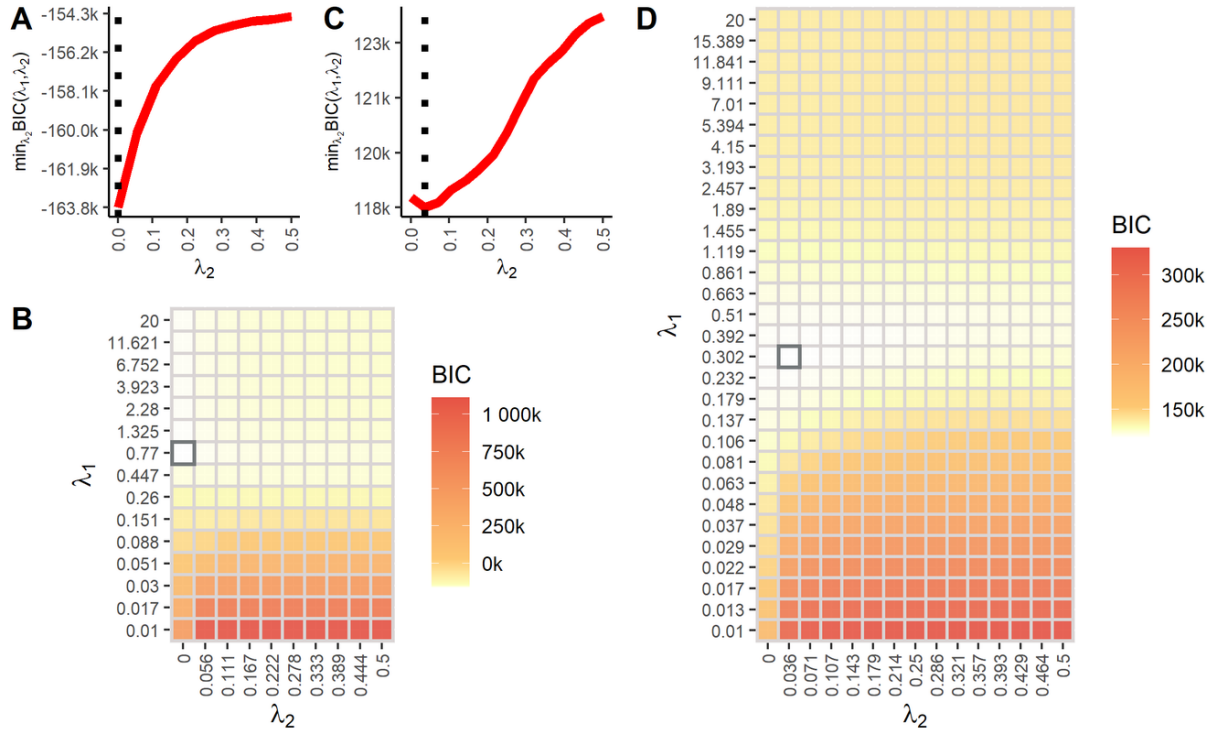


Figure 3: Grid searching of hyperparameters for graphical lasso model selection with ℓ_1 regularization. A and C shows the Bayesian information criterion (BIC) as a function of the second (λ_2) penalty for transcriptomic and metabolomic data sets, respectively. B and D are heatmaps displaying the complete grid search for the values of the tuning parameters λ_1 and λ_2 that minimize BIC, yielding parsimonious models for transcriptomic and metabolomics data sets, respectively.

396 For the gene expression data, λ_2 was optimized at $\lambda_2 = 0$. This implies different networks for each pedigree
 397 class with a different arrangement of non-zero positions for the gene expression data. On the other hand, for
 398 NMR data, the best combination of λ_1 and λ_2 that minimized the BIC found a small non-zero value for λ_2 ,
 399 implying a small level of similarity on the sparsity pattern across precision matrices for NMR data. Overall
 400 and across omic layers, the hybridization process generated substantial differences between pedigree classes
 401 and it seems to be better captured at the gene expression level.

402 Exploring lasso penalized precision matrices and network topologies

403 We detected 14 candidate modules for gene expression and 10 modules for metabolomic for the HR class
 404 (Figure 4). In the FL data sets, it was estimated 16 modules for gene expression and also 10 modules
 405 for metabolomics data. The modularity view of the gene-to-gene and metabolite-to-metabolite networks
 406 reveals the power-law distribution of node connections, where few vertices are highly connected whereas the
 407 majority has only one or few connecting edges. The organization of network structure based on modularity
 408 optimization allowed for the selection of intramodular hub nodes that are more likely to be involved in
 409 different biological pathways. Out of 70 hubs extracted from HR transcriptomic data (Figure 4A) and 80
 410 from FL transcriptomic data (Figure 4C), 30 genes (hubs) were conserved. These high-degree genes are
 411 located across all seven chromosomes, varying from two hubs on chromosome three up to 10 on chromosome
 412 two. Also, the degree of the hub gene set ranged from 34 to 182 edges. For metabolomic data, we found 32
 413 conserved hub nodes (Figure 4, B and D), all localized in one half of the NMR spectrum and with degrees

414 ranging from 52 to 357 edges.

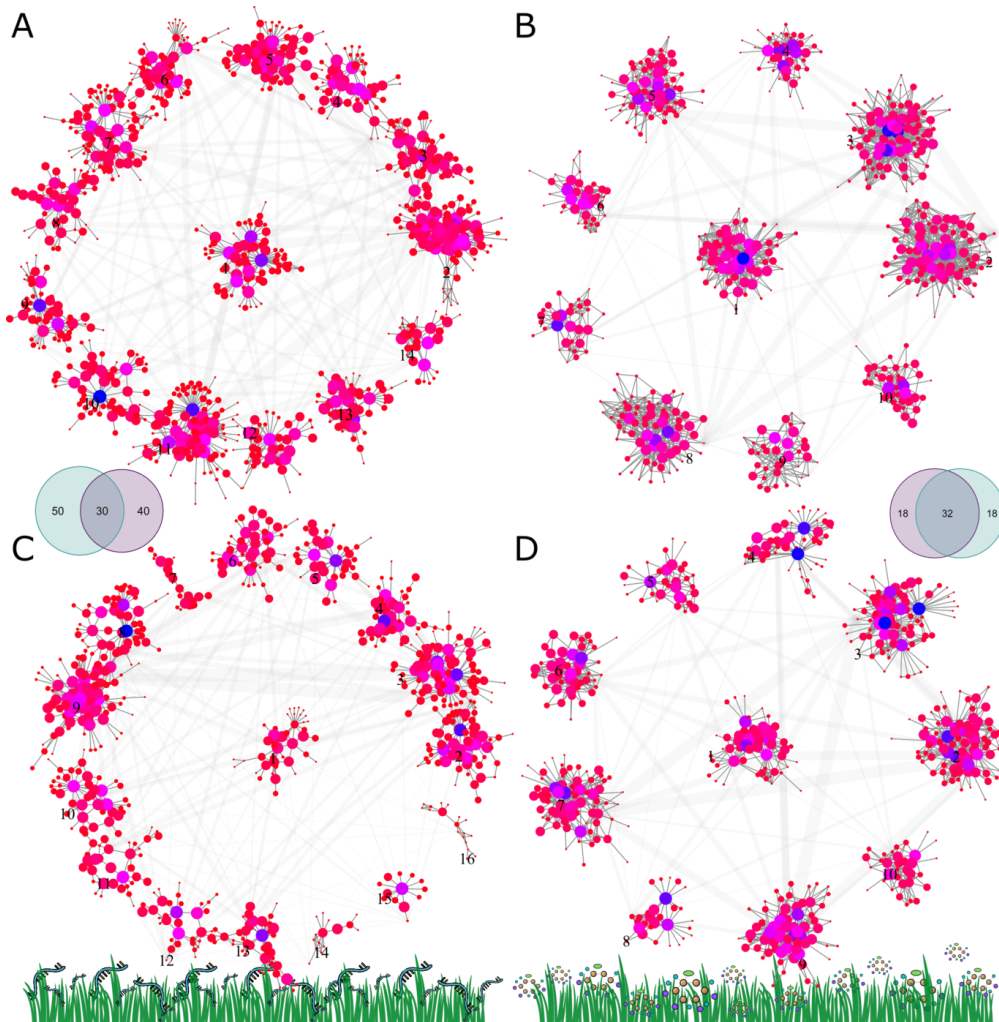


Figure 4: Abstract modularity view of the gene co-expression and metabolite networks constructed from gene expression data (A and C) and nuclear magnetic resonance (NMR) spectroscopy (B and D) for two data sets (A and B is the HR data set; C and D is the FL data set). Both node color and size reflect the hub score, i.e., the principal eigenvector of $\mathbf{A} \cdot t(\mathbf{A})$ matrix operation, where \mathbf{A} is the adjacency matrix of each graph. The color range goes from red for low-degree nodes to blue for highly connected ones. Edges between modules were collapsed and the width refers to the number of connections shared between any two modules. Venn diagrams show the overlap among sets of top hub features from each data set.

415 Integrative omics

416 The pairwise fitting of the multivariate genomic model revealed 21 significant edges between traits and omic
417 hub features after FDR correction (Figure 5). The multi-trait model was fitted 496 times but failed to
418 converge in 54 cases, possibly due to the variance component being close to zero. Therefore, five traits
419 displayed at least one significant edge with hub features in both pedigree classes. More edges can be seen on
420 the left side of the omics-phenotype network relative to the right side, which can be explained by the higher
421 heritability across traits in the FL data set (Supplemental Table S1) as well as overall higher heritability of

422 genomic features (Figure 2). Additionally, significant connections were found for six out of 30 hub genes and
 423 four out of 32 hub NMR variables. Three (hubs 16, 18, and 21) out of the six genes are located distantly
 424 apart on chromosome four whereas the remaining hubs 3, 7, and 22 are located on chromosomes one, two,
 425 and five, respectively. Genomic heritabilities of hubs displaying significant edges were considerably higher
 426 compared to the full feature space, with median h^2 twice as large. A closer look reveals a consistent pattern
 427 regarding the direction of the associations. Hub features positively or negatively associated with fiber content
 428 traits are also positively or negatively associated, respectively, to dry matter yield. The same holds true
 429 for protein content and digestibility traits, where associated hub features are inversely connected to fiber
 430 content. Additionally, the majority of hubs associated with phenotypes have more than one significant
 431 edge computed from independent analysis and, therefore, confirms the reliability of the estimated omics-
 432 phenotype network. We also fitted hub features as covariates in submodel 9 and computed the z-scores and
 433 associated p-values, which overall confirmed the results displayed in Figure 5 (data not shown). Finally, no
 434 hub feature had significant edges with traits from both pedigree classes, which can suggest steady genetic
 435 differences between classes and/or a lack of power to detect these shared genomic-based associations.

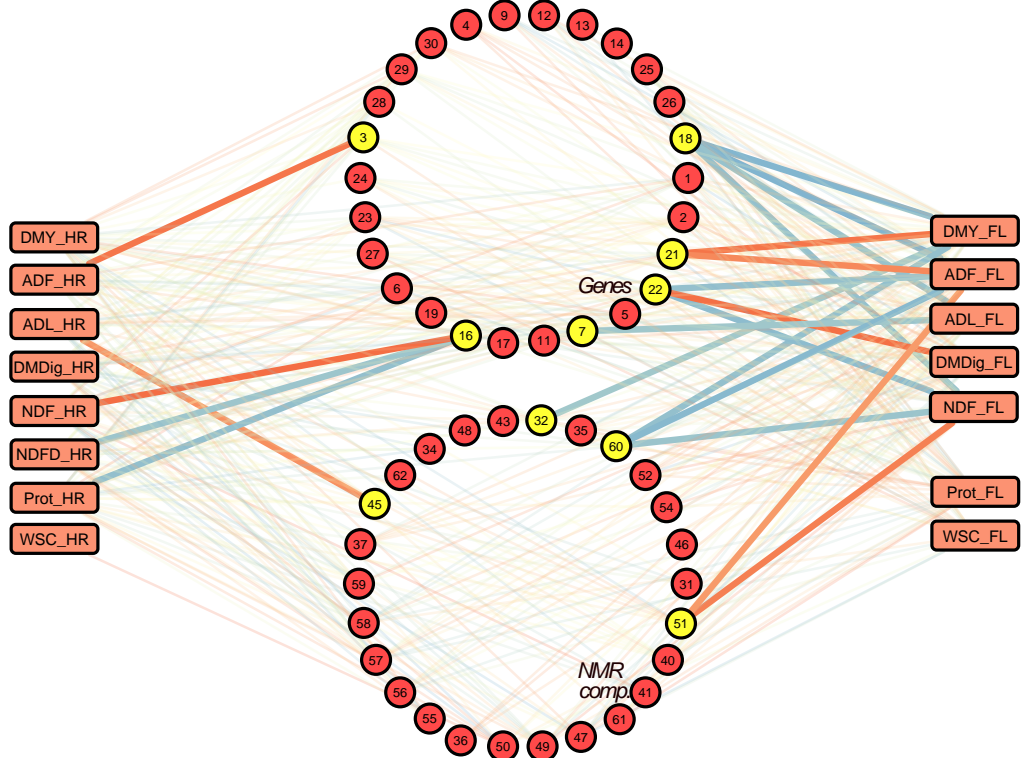


Figure 5: Weighted network linking hub omic features to phenotypes collected from family pools of two fodder grass pedigree classes (HR [hybrid ryegrass] data set on the left side and FL [*F. loliaceum*] data set on the right side). Edges represent the additive genetic correlation between omic features and traits and were built by the pair-wise fitting of a multivariate genomic model. Stronger edges in a gradient from red (negative) to blue (positive) colors represent false discovery rate corrected significant correlations at alpha 0.05. Highlighted omic nodes show at least one significant edge. DMY - dry matter yield; ADF - acid detergent fiber; ADL - acid detergent lignin; DMDig - digestible dry matter; NDF: -neutral detergent fiber; NDFD - digestible NDF; Prot - protein; and WSC - water-soluble carbohydrates.

436 Gene-set enrichment analysis revealed four gene ontology (GO) terms enriched in the set of 30 hub genes
437 displayed in Figure 5. Overrepresented GO terms were GO:0019438 (aromatic compound biosynthetic process),
438 GO:0018130 (heterocycle biosynthetic process), GO:1901362 (organic cyclic compound biosynthetic process),
439 and GO:0044271 (cellular nitrogen compound biosynthetic process). Bivariate mixed model analysis
440 revealed significant genetic correlations between the expression of gene hubs 18 and 21 and dry matter
441 yield. While hub gene 18 codes for the *atpF* gene (synthase subunit b, chloroplastic) and is associated
442 with energy production (GO:0015986 - proton motive force-driven ATP synthesis), the blast of biological
443 sequences revealed a putative unclassified retrotransposon protein originating from hub gene 21.

444 Omics-assisted predictions

445 Using gene expression data as an independent variable performed similarly to SNP-based marker predictions,
446 except for digestibility, protein, and neutral detergent fiber (Figure 6). Despite the overall poor prediction
447 performance across traits obtained when using NMR features as independent variables, the information
448 contained in this omic layer is useful for protein content prediction, with correlations above 0.4. Prediction
449 accuracy using only hub genes was compared with a second scenario where samples of the same size were
450 drawn from the whole predictor space aiming to check whether hub features carry asymmetrically more
451 (or less) information for prediction purposes. Overall, hub NMR variables appear to be more predictive of
452 nutritive quality traits than random samples of metabolomic features. On the other hand, results suggest
453 a weaker relationship between observed and predicted quality parameters using hub genes as regressors.
454 Finally, using the whole set of available predictors yields predominantly higher accuracies across traits.

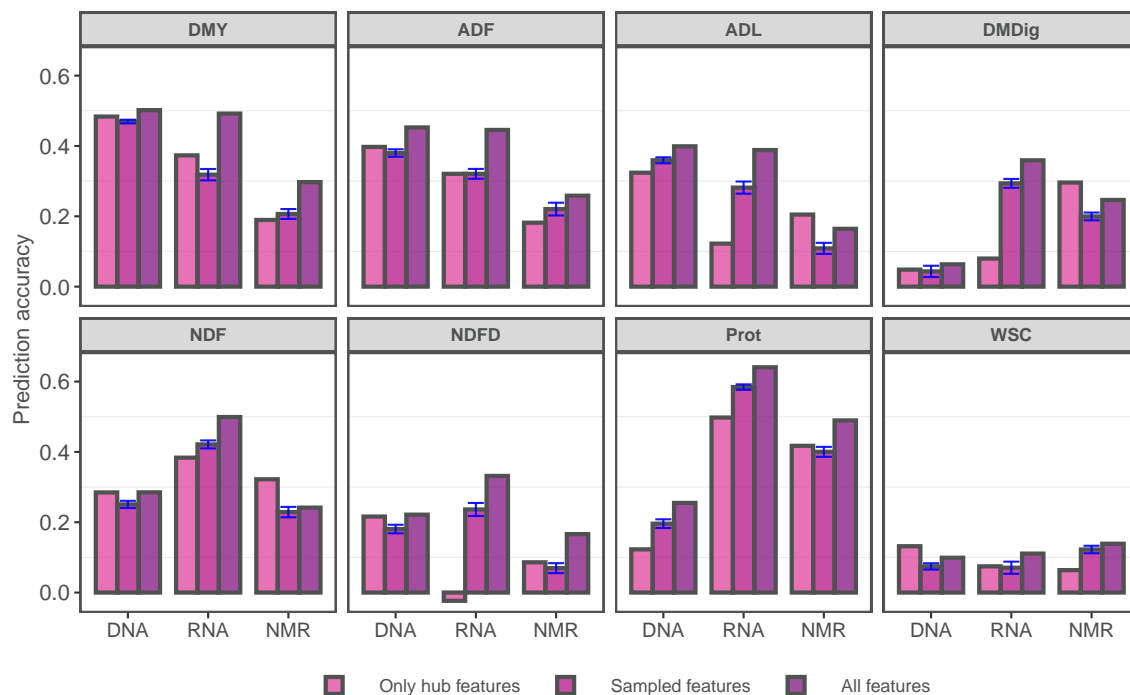


Figure 6: Random forest-based prediction accuracy computed for eight forage grass traits as a function of predictors encompassing three omic layers (DNA: SNP-based markers, RNA: gene expression via RNA-seq, and NMR: variables representing bucketed NMR spectra) and three predictor set configurations as indicated by the color gradient. The standard errors for the mean accuracy of sampled features are depicted in blue color. DMY - dry matter yield; ADF - acid detergent fiber; ADL - acid detergent lignin; DMDig - digestible dry matter; NDF: -neutral detergent fiber; NDFD - digestible NDF; Prot - protein; and WSC - water-soluble carbohydrates.

455 Discussion

456 The study elaborated here explores a network-based approach to combine multi-omic data arising from
457 an $n \ll p$ scenario, inferring associations between biomarker candidates with dry matter yield and nutritive
458 quality traits of polyploid forage grass families. This was accomplished by using a joint graphical lasso model
459 with a fused penalty for network reconstruction, followed by topological property extraction and integration
460 via multivariate mixed modeling. Further, a machine learning-based prediction scheme was explored to
461 verify the extent of information available in hubs and in the whole feature space for predicting agronomically
462 important phenotypes. The plant material consisted of family pools of inter-specific and- generic grass
463 hybrids from two connected diallels. Crossing different pasture species/genera is not a trivial task; obstacles
464 can emerge. Firstly, out of all initially planned crosses, only a subset generated viable seeds, impacting
465 the sample size. Also, seeds were not abundant for many of the crosses, requiring an additional year of
466 multiplication. Secondly, extraneous offspring patterns were detected, prompting a question of whether
467 normal parental contributions were formed for some of the F_2 families. This inquiry remained unanswered
468 in this manuscript given the complexity of the genetic material (family pools), SNPs called from RNA-seq
469 data, and the unavailability of parental genotypes. Despite the self-incompatibility (SI) ensuring cross-
470 pollination in perennial ryegrass (Croppano et al. 2021), four to eight percent of self-fertilization has been
471 reported (Arcioni and Mariotti 1983; Deniz and Dogru 2007). This, in addition to the low success rate of
472 inter-specific and- generic hybridization, might have caused the deviated genomic state of offspring families
473 for crosses that produced a small number of seeds. We did not use the parental information from the
474 diallel structure in the network construction but removed it by regression to control for the kinship among
475 individuals across analyses, a crucial action to avoid spurious results in network reconstruction. Due to the
476 genetic design, correlation among samples is expected, which can lead to the detection of co-expression among
477 features as a result of shared chromosomal segments. Additionally, confounding artifacts not controlled for
478 can affect groups of genes and NMR variables, which can lead to the detection of spurious correlations.
479 We fitted population structure as covariates by using principal component scores derived from the genetic
480 markers covering the whole genome aiming to alleviate the non-independence among samples, which has been
481 shown to reduce false network discoveries efficiently (Parsana et al. 2019). An extra layer of precaution to
482 avoid the effect of false-positive edges was deployed by retaining only common hub features between pedigree
483 classes.

484 The gene co-expression and metabolic networks as the ones we reconstructed in this study (Figure 4) using
485 RNA-seq and NMR variables, respectively, can contain interesting topological properties e.g., the existence
486 of highly connected nodes and the organization of nodes in modules (Li et al. 2015). We explored these
487 two properties aiming to select, across pedigree classes, conserved hubs extracted at a rate of five per
488 module, therefore, increasing the likelihood of sampling hubs associated with diverse biological processes.
489 Our approach to selecting and associating these features with phenotypic traits is altogether different from the
490 conventional method, which consists of performing a simple correlation-based gene co-expression network
491 analysis followed by thresholding to find modules that can then be summarized into a synthetic (eigen)
492 gene for association with external sample traits (Langfelder and Horvath 2008). As highlighted by other
493 authors (Huynh-Thu and Sanguinetti 2018; Jiang et al. 2019), this correlation-based approach cannot
494 distinguish between linear relationships due to directly dependent nodes and those arising from confounding
495 nodes, which might create spurious edges in the graph and, consequently, misleading clustering. In contrast,
496 Gaussian graphical models, as used here, are based on the precision (inverse variance) matrix and express
497 conditional dependence between pairs of features given all the other variables in the data set (Danaher et al.
498 2014) which, therefore, avoids declaring an edge when no causal relationship exists. Regarding the presence
499 and distribution of edges across reconstructed networks, the proportion of undirected edges given the total
500 available nodes was much higher for the NMR -based metabolic network relative to the gene expression
501 graph. This is a consequence of the lack of independence among bins closely located across the NMR
502 spectrum. Indeed, an average autocorrelation across samples revealed significant spikes up to lag 12 (data

503 not shown). Therefore, a proper feature selection algorithm for spectral data can be implemented to deal
504 with the existence of autocorrelation.

505 Picturing a biological regulatory cascade, hub genes are usually regulatory factors located upstream, whereas
506 genes represented by low-degree nodes are located on the other end (Zeng et al. 2022). They can be associated
507 with biological processes from which several others are dependent, yielding the commonly observed power-
508 law degree distribution. The presence of a limited amount of important hub genes, however, does not
509 necessarily imply a simple genetic architecture, because the regulation of the hub gene expression is typically
510 highly polygenic. Investigating putative hubs can reveal important genes as, for example, the cold-regulated
511 gene *Lolium perenne LIR1* (*LpLIR1*) (Ciannamea et al. 2007) represented by the hub gene coded as 22 in
512 Figure 5, which is located at chr5:155166187-155167265 in the *L. perenne* genome and appears to act in the
513 photoperiodic regulation of flowering. Another example is hub 7, which represents the *PDX1.1* gene, involved
514 in the biosynthesis of vitamin B6 and protection against stresses (Liu et al. 2022). Overexpression of PDX
515 proteins was shown to increase seed size and biomass in Arabidopsis (Raschke et al. 2011). For metabolite-
516 metabolite networks, high-degree nodes may represent signaling molecules or molecules engaged in many
517 reactions. The content and diversity of such molecules have been shown to be shaped by domestication as
518 well as due to crop improvement (Alseekh et al. 2021). Improving biomass output per area is the ultimate
519 breeding goal in a forage breeding program and also implies selection pressure for stress endurance due to
520 animal grazing or mechanical harvesting. In this sense, secondary metabolites are well-known for their role
521 in the plant's response to external disturbances as herbivory (Degenhardt Jorg 2009). In more general,
522 significant associations can be detected between metabolites and agronomic traits (Turner et al. 2016) and
523 the whole NMR spectrum can be used for metabolomic-assisted prediction (Guo et al. 2022). That being
524 stated, genetic selection for elite grasses might be linked to an altered profile of metabolites, leveraging their
525 usefulness as markers for selection or for prediction purposes. Indeed, great chemical diversity is available
526 in perennial ryegrass (Subbaraj et al. 2019), not only adding another layer of information for omics-assisted
527 breeding but also enabling target improvement of varieties with a specific profile of key metabolites.

528 Together, significant additive genetic correlations between omic features and phenotypic traits displayed in
529 Figure 5 and the presence of over-represented gene ontology (GO) terms in the hub gene set supports the
530 evidence that these features hold fundamental biological properties. We further assessed the predictive power
531 available in the sets of gene and metabolite hubs. This was accomplished by merging the HR and FL data
532 sets for trait prediction aiming to increase the sample size, which even though still below the appropriate size
533 for genomic selection was counterbalanced by a high signal-to-noise ratio given the diallel structure which
534 is expected to boost information for model learning (see Figure 1). Splitting between training and testing
535 sets would reduce the sample size for training. Therefore, we used the ensemble learning method of random
536 forest with all samples and reported the out-of-bag (OOB) accuracy as a prediction performance metric,
537 eliminating the need to set aside a test set (Breiman 2001). Despite the crossing scheme, eigenvectors from
538 marker data did not reveal large dissimilarity between pedigree classes (Supplemental Figure S1), therefore
539 allowing for the joint analysis. Also, random forest is not very sensitive to hyperparameter tuning (Probst et
540 al. 2019), making it a good option for the designed prediction setup. This can be attested by the magnitude
541 of predictions displayed in Figure 6. Prediction accuracy for dry matter yield was reported in other studies at
542 0.31 using diploid ryegrass synthetic populations (Pembleton et al. 2018), 0.34 using tetraploid ryegrass (Guo
543 et al. 2018), and 0.5 investigating diploid perennial ryegrass (Aroju et al. 2020). Here, we report values
544 of prediction accuracy of dry matter yield that approximate 0.5 (Figure 6) using both SNP-markers and
545 gene expression, despite the lower sample size but helped by high relatedness among samples, an important
546 component in genomic selection (Edwards et al. 2019). Also for dry matter yield, surprisingly the most
547 heritable trait (Supplemental Table S1), the set of hub genes and SNPs markers tagging them seem more
548 predictive than features sampled at random. For the remaining traits, mixed results were observed which
549 can be an artifact due to sample size, low heritability, or population structure. Additionally, the signal
550 might be dependent on the genetic background and disappeared as we merged the two data sets for the
551 prediction study. Heritability is an important parameter driving prediction accuracy. If it is low, the error
552 variance will be higher, leading to difficulties in estimating the effect of genome segments accurately (van der

553 Werf 2013), especially if the sample size is not sufficiently large. Small values of heritability were primarily
554 observed for quality traits (supplemental Table S1), which explains the lack of predictive power of the model
555 for digestibility, water-soluble carbohydrates, and digestible NDF, for example. The NIR-based quality
556 parameters are obtained from calibrated models using data of chemical analysis from samples of standard
557 breeding materials and might not translate well into curves of inter-generic and- species hybrids, explaining
558 the lower heritability.

559 Given that plant tissues were sampled once from pools of seedlings grown in a greenhouse environment at
560 the F₂ generation for transcriptomic and metabolomic analyses, the information carried by the recorded
561 features represents a snapshot of the complex interactome at that particular condition in space, time, and
562 random mating generation. This information was learned by the model and translated into higher prediction
563 accuracy for protein and digestibility, despite the fact that phenotypes were recorded in later growth stages
564 and in another generation of random mating. Across omic layers, the results also showed that using all
565 available features is almost always a better choice for increased prediction accuracy. Besides more main
566 effects being captured, the random forest model can capture feature-feature interactions (Yao et al. 2013)
567 as long as the marginal effects are large enough to cause a tree split, therefore, accounting for some of the
568 existing epistasis. Therefore, the existence of significant edges displayed in Figure 5 and the magnitude of the
569 prediction accuracies presented in Figure 6 reveals a strong link between field-based phenotypes and heritable
570 omic features assessed from young seedlings in a controlled environment. Altogether, this information brings
571 the question of whether phenotypes from seedlings grown for DNA sampling could be recorded through a
572 low-cost NIR-based method and used to improve the accuracy of genomic selection models, a subject worthy
573 of consideration in future research.

574 The use of multi-omics in plant breeding-related studies is becoming more popular due to decreasing in cost
575 per data point as a result of modern high-throughput technologies. This has been allowing researchers to
576 reconstruct complex biological networks for inference and mining. Out of the many topological properties
577 that can be retrieved from an interaction network, hub features showing many putative links have been
578 shown to play important biological roles in plants (Tahmasebi et al. 2019). Our study reveals that narrowing
579 down the high-dimensional feature space generated by high-throughput omic analysis to fewer entities by
580 leveraging properties of the graphical theory can reveal important biomolecules for molecular studies and
581 breeding. Additionally, dimensionality reduction can substantially boost detection power by alleviating the
582 multiple testing problem. Further investigations of candidate features may help elucidate biological processes
583 underlying the expression of phenotypic traits and serve as markers for omics-assisted selection in breeding
584 programs. Even though we did not perform compound identification from the NMR data, this is a feasible
585 task and may reveal metabolites playing important roles in biomass yield and nutritional quality.

586 Conclusion

587 The scientific community has seen a sharp increase in publications exploring the usefulness of biological
588 network reconstruction based on high throughput omics data since the 2000s, but studies with forage species
589 remain scarce. Here, we have explored the usefulness of topological properties of gene co-expression and
590 metabolic networks in explaining the phenotypic variance of eight traits assessed in family pools of inter-
591 specific and -generic grass hybrids. Network topology estimated via fused graphical lasso revealed profound
592 network differences between pedigree classes, but a set of 30 high-degree hub genes and 32 hub NMR variables
593 remained conserved across classes given the selection criteria, out of which 10 hubs were found as candidate
594 biomolecules significantly associated with the expression of agronomic phenotypes. Gene set enrichment
595 analysis and weighted omics-phenotype network estimation suggested that sets of hubs are likely to contain
596 essential features modulating interactomes and the expression of economically important phenotypes.

597 Acknowledgments

598 This work was supported by the Innovation Fund Denmark, through the project Breed4Biomass (grant
599 6150-00020B). The authors gratefully acknowledge the financial support provided by the aforementioned
600 organization. The authors declare no competing interests.

601 Author contribution statement

602 EB conceptualized the study, wrote the code for analyses and data visualizations, interpreted the results, and
603 drafted the manuscript. DF contributed to the conception and design of the B4B project and data curation.
604 IN contributed to omics data generation and miscellaneous bioinformatics analyses. IL contributed with
605 bioinformatics expertise and project design. MG created the populations, carried out field trials, and recorded
606 agronomic phenotypes. TD converted NIR spectrums into nutritive quality parameters. CSJ, TA, and LJ
607 contributed to the conception and design of the B4B project and funding acquisition. TA acquired funding
608 for and coordinated the B4B project. LJ supervised the current study and provided valuable comments. All
609 authors critically reviewed the manuscript. All authors have read and approved the manuscript.

610 Data availability statement

611 The omics data sets supporting the conclusions of this article have been made available through an
612 R data package named “breed4biomass”, which is openly available on GitHub (<https://github.com/elesandrobornhofen/breed4biomass>).
613

614 References

- 615 Akiyama Y, Kimura K, Yamada-Akiyama H, and others (2012) Genomic characteristics of a diploid F4
616 festulolium hybrid (*Lolium multiflorum* × *Festuca arundinacea*). *Genome* 55:599–603. <https://doi.org/10.1139/g2012-048>
- 618 Alseekh S, Scossa F, Wen W, and others (2021) Domestication of Crop Metabolomes: Desired and Unin-
619 tended Consequences. *Trends in Plant Science* 26:650–661. <https://doi.org/10.1016/j.tplants.2021.02.005>
- 621 Arcioni S, Mariotti D (1983) Selfing and interspecific hybridization in *Lolium perenne* L. and *Lolium mul-*
622 *tiflorum* Lam. evaluated by phosphoglucoisomerase as isozyme marker. *Euphytica* 32:33–40. <https://doi.org/10.1007/bf00036861>
- 624 Arojju SK, Cao M, Trolove M, and others (2020) Multi-trait genomic prediction improves predictive ability
625 for dry matter yield and water-soluble carbohydrates in perennial ryegrass. *Frontiers in Plant Science* 11.
626 <https://doi.org/10.3389/fpls.2020.01197>
- 627 Ashraf BH, Jensen J, Asp T, Janss LL (2014) Association studies using family pools of outcrossing crops
628 based on allele-frequency estimates from DNA sequencing. *Theoretical and Applied Genetics* 127:1331–1341.
629 <https://doi.org/10.1007/s00122-014-2300-4>
- 630 Augugliaro L, Mineo AM, Wit EC (2016) ℓ_1 -penalized methods in high-dimensional Gaussian Markov random
631 fields. In: *Computational Network Analysis* with R. John Wiley & Sons, Ltd.
- 632 Bartzis G, Deelen J, Maia J, and others (2017) Estimation of metabolite networks with regard to a specific
633 covariable: applications to plant and human data. *Metabolomics* 13. <https://doi.org/10.1007/s11306-017-1263-2>
- 635 Benjamini Y, Hochberg Y (1995) Controlling the False Discovery Rate: A Practical and Powerful Approach
636 to Multiple Testing. *Journal of the Royal Statistical Society: Series B (Methodological)* 57:289–300. <https://doi.org/10.1111/j.2517-6161.1995.tb02031.x>

- 638 Bersanelli M, Mosca E, Remondini D, and others (2016) Methods for the integration of multi-omics data:
639 mathematical aspects. *BMC Bioinformatics* 17. <https://doi.org/10.1186/s12859-015-0857-9>
- 640 Blondel VD, Guillaume J-L, Lambiotte R, Lefebvre E (2008) Fast unfolding of communities in large networks.
641 *Journal of Statistical Mechanics: Theory and Experiment* 2008:P10008. <https://doi.org/10.1088/1742-5468/2008/10/p10008>
- 643 Bo V, Curtis T, Lysenko A, and others (2014) Discovering Study-Specific Gene Regulatory Networks. *PLoS ONE* 9:e106524. <https://doi.org/10.1371/journal.pone.0106524>
- 645 Breiman L (2001) Random Forests. *Machine Learning* 45:5–32. <https://doi.org/10.1023/a:1010933404324>
- 647 Cericola F, Lenk I, Fè D, and others (2018) Optimized use of low-depth genotyping-by-sequencing for genomic
648 pPrediction among multi-parental family pools and single plants in perennial ryegrass (*Lolium perenne* L.).
649 *Frontiers in Plant Science* 9. <https://doi.org/10.3389/fpls.2018.00369>
- 650 Chen P, Liu P, Zhang Q, and others (2021) Gene coexpression network analysis indicates that hub genes
651 related to photosynthesis and starch synthesis modulate salt stress tolerance in *Ulmus pumila*. *International
652 Journal of Molecular Sciences* 22:4410. <https://doi.org/10.3390/ijms22094410>
- 653 Ciannamea S, Jensen CS, Agerskov H, and others (2007) A new member of the *LIR* gene family from perennial
654 ryegrass is cold-responsive and promotes vegetative growth in *Arabidopsis*. *Plant Science* 172:221–227.
655 <https://doi.org/10.1016/j.plantsci.2006.08.011>
- 656 Crombach A, Hogeweg P (2008) Evolution of evolvability in gene regulatory networks. *PLoS Computational
657 Biology* 4:e1000112. <https://doi.org/10.1371/journal.pcbi.1000112>
- 658 Cropano C, Manzanares C, Yates S, and others (2021) Identification of candidate genes for self-compatibility
659 in perennial ryegrass (*Lolium perenne* L.). *Frontiers in Plant Science* 12. <https://doi.org/10.3389/fpls.2021.707901>
- 661 Csardi G, Nepusz T (2006) The igraph software package for complex network research. *InterJournal Complex
662 Systems*:1695
- 663 Danaher P, Wang P, Witten DM (2014) The joint graphical lasso for inverse covariance estimation across
664 multiple classes.. *J R Stat Soc Series B Stat Methodol* 76:373–397. <https://doi.org/10.1111/rssb.12033>
- 665 Degenhardt Jorg (2009) Indirect defense responses to herbivory in grasses. *Plant Physiology* 149:96–102.
666 <https://doi.org/10.1104/pp.108.128975>
- 667 Deniz B, Dogru U (2007) Interspecific hybridisation in *Lolium* evaluated by morphological genetic
668 markers. *New Zealand Journal of Agricultural Research* 50:279–284. <https://doi.org/10.1080/00288230709510295>
- 670 Edwards SMK, Buntjer JB, Jackson R, and others (2019) The effects of training population design on genomic
671 prediction accuracy in wheat. *Theoretical and Applied Genetics*. <https://doi.org/10.1007/s00122-019-03327-y>
- 673 Friedman J, Hastie T, Tibshirani R (2007) Sparse inverse covariance estimation with the graphical lasso.
674 *Biostatistics* 9:432–441. <https://doi.org/10.1093/biostatistics/kxm045>
- 675 Fè D, Cericola F, Byrne S, and others (2015) Genomic dissection and prediction of heading date in perennial
676 ryegrass. *BMC Genomics* 16: <https://doi.org/10.1186/s12864-015-2163-3>
- 677 Garrison E, Marth G (2012) Haplotype-based variant detection from short-read sequencing.
678 arXiv:1207.3907v2. <https://doi.org/10.48550/arXiv.1207.3907>
- 679 Gilmour AR, Gogel BJ, Cullis BR, and others (2015) ASReml user guide release 4.1 structural specification.
680 Hemel hempstead: VSN international ltd.

- 681 Glombik M, Copetti D, Bartos J, and others (2021) Reciprocal allopolyploid grasses (*Festuca* × *Lolium*)
682 display stable patterns of genome dominance. 107:1166–1182. <https://doi.org/10.1111/tpj.15375>
- 683 Guo X, Cericola F, Fè D, and others (2018) Genomic prediction in tetraploid ryegrass using allele frequencies
684 based on genotyping by sequencing. Frontiers in Plant Science 9. <https://doi.org/10.3389/fpls.2018.01165>
- 686 Guo X, Jahoor A, Jensen J, Sarup P (2022) Metabolomic spectra for phenotypic prediction of malting quality
687 in spring barley. Scientific Reports 12. <https://doi.org/10.1038/s41598-022-12028-4>
- 688 Hollender CA, Kang C, Darwish O, and others (2014) Floral transcriptomes in woodland strawberry uncover
689 developing receptacle and anther gene networks. Plant Physiology 165:1062–1075. <https://doi.org/10.1104/pp.114.237529>
- 691 Hu G, Hovav R, Grover CE, and others (2017) Evolutionary conservation and divergence of gene coexpression
692 networks in *Gossypium* (Cotton) seeds. Genome Biology and Evolution evw280. <https://doi.org/10.1093/gbe/evw280>
- 694 Huynh-Thu VA, Sanguinetti G (2018) Gene regulatory network inference: an introductory survey. In:
695 Methods in Molecular Biology. 1883:1-23. https://doi.org/10.1007/978-1-4939-8882-2_1
- 696 Jacob D, Deborde C, Lefebvre M, and others (2017) NMRProcFlow: a graphical and interactive tool dedicated
697 to 1D spectra processing for NMR-based metabolomics. Metabolomics 13. <https://doi.org/10.1007/s11306-017-1178-y>
- 699 Jiang D, Armour CR, Hu C, and others (2019) Microbiome multi-omics network analysis: statistical considerations
700 limitations, and opportunities. Frontiers in Genetics 10. <https://doi.org/10.3389/fgene.2019.00995>
- 702 Jones P, Binns D, Chang H-Y, and others (2014) InterProScan 5: genome-scale protein function classification.
703 Bioinformatics 30:1236–1240. <https://doi.org/10.1093/bioinformatics/btu031>
- 704 Kapoor R, Datta A, Thomson M (2021) Fused graphical lasso recovers flowering time mutation genes in
705 *Arabidopsis thaliana*. Inventions 6:52. <https://doi.org/10.3390/inventions6030052>
- 706 Keep T, Sampoux J-P, Blanco-Pastor JL, and others (2020) High-throughput genome-wide genotyping to
707 optimize the use of natural genetic resources in the grassland species perennial ryegrass (*Lolium perenne* L.).
708 G3 Genes|Genomes|Genetics 10:3347–3364. <https://doi.org/10.1534/g3.120.401491>
- 709 Kim D, Paggi JM, Park C, and others (2019) Graph-based genome alignment and genotyping with HISAT2
710 and HISAT-genotype. Nature Biotechnology 37:907–915. <https://doi.org/10.1038/s41587-019-0201-4>
- 711 Kleinberg JM (1999) Authoritative sources in a hyperlinked environment. Journal of the ACM 46:604–632.
712 <https://doi.org/10.1145/324133.324140>
- 713 Klopfenstein DV, Zhang L, Pedersen BS, and others (2018) GOATOOLS: A Python library for Gene Ontology
714 analyses. Scientific Reports 8: <https://doi.org/10.1038/s41598-018-28948-z>
- 715 Kopecký D, Šimoníková D, Ghesquière M, Doležel J (2017) Stability of Genome Composition and Recombination
716 between Homoeologous Chromosomes in *Festulolium* (*Festuca* × *Lolium*) Cultivars. Cytogenetic and
717 Genome Research 151:106–114. <https://doi.org/10.1159/000458746>
- 718 Langfelder P, Horvath S (2008) WGCNA: an R package for weighted correlation network analysis. BMC
719 Bioinformatics 9: <https://doi.org/10.1186/1471-2105-9-559>
- 720 Li Y, Jackson SA (2015) Gene network reconstruction by integration of prior biological knowledge. G3
721 Genes|Genomes|Genetics 5:1075–1079. <https://doi.org/10.1534/g3.115.018127>
- 722 Li Y, Pearl SA, Jackson SA (2015) Gene networks in plant biology: approaches in reconstruction and analysis.
723 Trends in Plant Science 20:664–675. <https://doi.org/10.1016/j.tplants.2015.06.013>

- 724 Liu W, He G, Deng XW (2021) Biological pathway expression complementation contributes to biomass
725 heterosis in *Arabidopsis*. Proceedings of the National Academy of Sciences 118. <https://doi.org/10.1073/pnas.2023278118>
- 727 Liu W, Wang Q, Chang J, and others (2022) Circulatory metabolomics reveals the association of the metabolites
728 with clinical features in the patients with intrahepatic cholestasis of pregnancy. Frontiers in Physiology
729 13. <https://doi.org/10.3389/fphys.2022.848508>
- 730 Liu Y, Maniero RA, Giehl RFH, and others (2022) *PDX1.1*-dependent biosynthesis of vitamin B6 protects
731 roots from ammonium-induced oxidative stress. Molecular Plant 15:820–839. <https://doi.org/10.1016/j.molp.2022.01.012>
- 733 Madsen P, Jensen J (2013) A user's guide to DMU-A package for analysing multivariate mixed models.
734 Version 6, Release 5.2. <https://dmu.ghpc.au.dk/dmu/DMU/Doc/Current/>
- 735 Mayer M (2021) missRanger: Fast Imputation of Missing Values <https://github.com/mayer79/missRanger>
- 737 Meyer TD, Sinnaeve D, Gasse BV, and others (2008) NMR-based characterization of metabolic alterations in
738 hypertension using an adaptive intelligent binning algorithm. Analytical Chemistry 80:3783–3790. <https://doi.org/10.1021/ac7025964>
- 740 Nagy I, Veeckman E, Liu C, and others (2022) Chromosome-scale assembly and annotation of the perennial
741 ryegrass genome. BMC Genomics 23. <https://doi.org/10.1186/s12864-022-08697-0>
- 742 Nantongo JS, Potts BM, Davies NW, and others (2021) Additive genetic variation in *Pinus radiata* bark
743 chemistry and the chemical traits associated with variation in mammalian bark stripping. Heredity
744 127:498–509. <https://doi.org/10.1038/s41437-021-00476-z>
- 745 Naserkheil M, Ghafouri F, Zakizadeh S, and others (2022) Multi-omics integration and network analysis
746 reveal potential hub genes and genetic mechanisms regulating bovine mastitis. Current Issues in Molecular
747 Biology 44:309–328. <https://doi.org/10.3390/cimb44010023>
- 748 Parsana P, Ruberman C, Jaffe AE, and others (2019) Addressing confounding artifacts in reconstruction of
749 gene co-expression networks. Genome Biology 20. <https://doi.org/10.1186/s13059-019-1700-9>
- 750 Pembleton LW, Inch C, Baillie RC, and others (2018) Exploitation of data from breeding programs supports
751 rapid implementation of genomic selection for key agronomic traits in perennial ryegrass. Theoretical and
752 Applied Genetics 131:1891–1902. <https://doi.org/10.1007/s00122-018-3121-7>
- 753 Pereira-Leal JB, Audit B, Peregrin-Alvarez JM, Ouzounis CA (2004) An exponential core in the heart of
754 the yeast protein interaction network. Molecular Biology and Evolution 22:421–425. <https://doi.org/10.1093/molbev/msi024>
- 756 Pertea M, Pertea GM, Antonescu CM, and others (2015) StringTie enables improved reconstruction of a
757 transcriptome from RNA-seq reads. Nature Biotechnology 33:290–295. <https://doi.org/10.1038/nbt.3122>
- 759 Pignon CP, Fernandes SB, Valluru R, and others (2021) Phenotyping stomatal closure by thermal imaging
760 for GWAS and TWAS of water use efficiency-related genes. Plant Physiology 187:2544–2562. <https://doi.org/10.1093/plphys/kiab395>
- 762 Probst P, Boulesteix AL, Bischl B (2019) Tunability: Importance of Hyperparameters of machine learning
763 algorithms. Journal of Machine Learning Research 20(53):132. <http://jmlr.org/papers/v20/18-444.html>
- 765 Raschke M, Boycheva S, Crèvecoeur M, and others (2011) Enhanced levels of vitamin B6 increase aerial
766 organ size and positively affect stress tolerance in *Arabidopsis*. The Plant Journal 66:414–432. <https://doi.org/10.1111/j.1365-313x.2011.04499.x>

- 768 Schwarz G (1978) Estimating the dimension of a model. The Annals of Statistics 6(2):461-464. <https://www.jstor.org/stable/2958889>
- 770 Self SG, Liang K-Y (1987) Asymptotic properties of maximum likelihood estimators and likelihood ratio
771 tests under nonstandard conditions. Journal of the American Statistical Association 82:605–610. <https://doi.org/10.1080/01621459.1987.10478472>
- 773 Shahdoust M, Mahjub H, Pezeshk H, Sadeghi M (2019) A network-based comparison between molecular
774 apocrine breast cancer tumor and basal and luminal tumors by joint graphical lasso. IEEE/ACM Transactions
775 on Computational Biology and Bioinformatics 1–1. <https://doi.org/10.1109/tcbb.2019.2911074>
- 776 Shannon P, Markiel A, Ozier O, and others (2003) Cytoscape: A software environment for integrated models
777 of biomolecular interaction networks. Genome Research 13:2498–2504. <https://doi.org/10.1101/gr.1239303>
- 779 Subbaraj AK, Huege J, Fraser K, and others (2019) A large-scale metabolomics study to harness chemical
780 diversity and explore biochemical mechanisms in ryegrass. Communications Biology 2. <https://doi.org/10.1038/s42003-019-0289-6>
- 782 Tahmasebi A, Ashrafi-Dehkordi E, Shahriari AG, and others (2019) Integrative meta-analysis of transcriptomic
783 responses to abiotic stress in cotton. Progress in Biophysics and Molecular Biology 146:112–122.
784 <https://doi.org/10.1016/j.pbiomolbio.2019.02.005>
- 785 Tripathi S, Dehmer M, Emmert-Streib F (2014) NetBioV: an R package for visualizing large network data in
786 biology and medicine. Bioinformatics 30:2834–2836. <https://doi.org/10.1093/bioinformatics/btu384>
- 787 Turner MF, Heuberger AL, Kirkwood JS, and others (2016) Non-targeted metabolomics in diverse sorghum
788 breeding lines indicates primary and secondary metabolite profiles are associated with plant biomass accumulation
789 and photosynthesis. Frontiers in Plant Science 7. <https://doi.org/10.3389/fpls.2016.00953>
- 790 VanRaden PM (2008) Efficient methods to compute genomic predictions.. J Dairy Sci 91:4414–23
- 791 Wen W, Li D, Li X, and others (2014) Metabolome-based genome-wide association study of maize kernel
792 leads to novel biochemical insights. Nature Communications 5. <https://doi.org/10.1038/ncomms4438>
- 793 Wickham H (2016) ggplot2: elegant graphics for data analysis. Springer-Verlag New York. <https://doi.org/10.1007/978-0-387-98141-3>
- 795 Wright MN, Ziegler A (2017) ranger: A fast implementation of random forests for high dimensional data in
796 C++ and R. Journal of Statistical Software 77:1–17. <https://doi.org/10.18637/jss.v077.i01>
- 797 Wu M-Y, Dai D-Q, Zhang X-F, Zhu Y (2013) Cancer subtype discovery and biomarker identification via
798 a new robust network clustering algorithm. PLoS ONE 8:e66256. <https://doi.org/10.1371/journal.pone.0066256>
- 800 Yan Q, Li J, Lu L, and others (2022) Comparative transcriptome study of the elongating internode in
801 elephant grass (*Cenchrus purpureus*) seedlings in response to exogenous gibberellin applications. Industrial
802 Crops and Products 178:114653. <https://doi.org/10.1016/j.indcrop.2022.114653>
- 803 Yao C, Spurlock DM, Armentano LE, and others (2013) Random Forests approach for identifying additive
804 and epistatic single nucleotide polymorphisms associated with residual feed intake in dairy cattle. Journal
805 of Dairy Science 96:6716–6729. <https://doi.org/10.3168/jds.2012-6237>
- 806 Zeng Z, Zhang S, Li W, and others (2022) Gene-coexpression network analysis identifies specific modules
807 and hub genes related to cold stress in rice. BMC Genomics 23. <https://doi.org/10.1186/s12864-022-08438-3>
- 809 Zhang X, Pang J, Ma X, and others (2019) Multivariate analyses of root phenotype and dynamic trans-
810 scriptome underscore valuable root traits and water-deficit responsive gene networks in maize. Plant Direct

- 811 3:e00130. <https://doi.org/10.1002/pld3.130>
- 812 Zheng Y, Wang N, Zhang Z, and others (2022) Identification of flowering regulatory networks and hub genes
813 expressed in the leaves of *Elymus sibiricus* L. using comparative transcriptome analysis. *Frontiers in Plant
814 Science* 13. <https://doi.org/10.3389/fpls.2022.877908>
- 815 de Steenhuijsen PWA, Heinonen S, Hasrat R, and others (2016) Nasopharyngeal microbiota, host transcrip-
816 tome, and disease severity in children with respiratory syncytial virus infection.. *Am J Respir Crit Care
817 Med* 194:1104–1115. <https://doi.org/10.1164/rccm.201602-02200C>
- 818 e Lima FA, Li K, Wen W, and others (2018) Unraveling lipid metabolism in maize with time-resolved
819 multi-omics data. *The Plant Journal* 93:1102–1115. <https://doi.org/10.1111/tpj.13833>
- 820 van der Werf J (2013) Genomic selection in animal breeding programs. In: *Methods in Molecular Biology*.
821 Humana Press, pp 543–561. https://doi.org/10.1007/978-1-62703-447-0_26

822 Supplemental Material

823 Supplemental figures

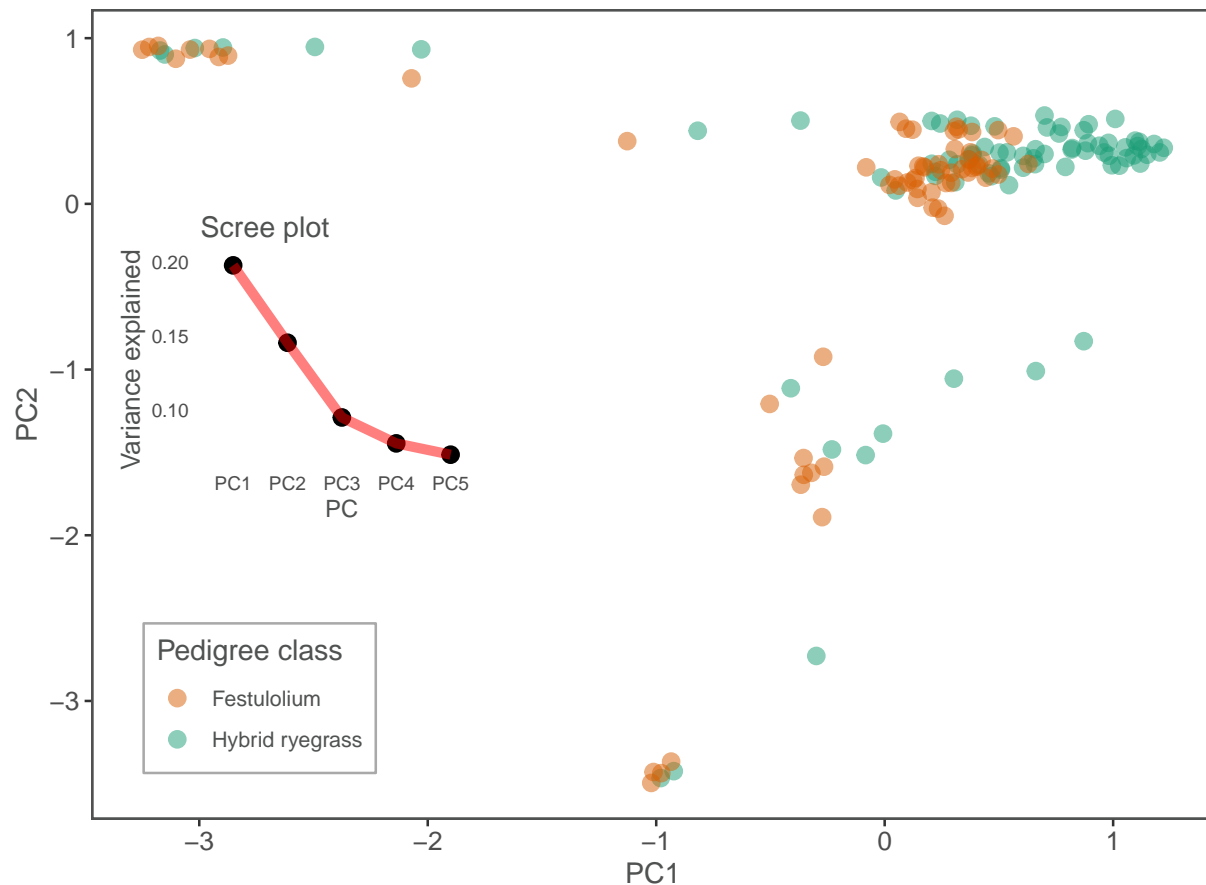


Figure S1: Scatter plot displaying scores of the first two principal components (PCs) from the PC analysis of the combined (hybrid ryegrass plus *Festulolium loliaceum* samples) genomic relationship matrix. The number of samples is equal to 144. An overlaying scree plot shows the variance explained by the first five PCs.

824 **Supplemental tables**

Table S1: Restricted maximum likelihood (REML) estimation of variance components from two field trials comprising different pedigree classes of forage grasses: HR - hybrid ryegrass and FL - *Festulolium loliaceum*.

Ped. class	Variance component	Traits ¹							
		DMY	ADF	ADL	DMDig	NDF	NDFD	Prot	WSC
HR	σ_u^2	2181.088	0.125	0.002	0.135	0.278	1.451	0.186	0.000
	S.E.	1054.606	0.073	0.002	0.086	0.174	0.741	0.113	0.368
FL	σ_u^2	7353.689	0.260	0.018	0.148	0.590	0.000	0.034	0.194
	S.E.	3090.586	0.128	0.011	0.281	0.277	0.540	0.046	0.162
HR	σ_f^2	0.000	0.000	0.000	0.031	0.029	0.000	0.000	0.269
	S.E.	892.753	0.075	0.002	0.099	0.183	0.859	0.117	0.587
FL	σ_f^2	0.000	0.000	0.000	0.374	0.102	0.704	0.071	0.000
	S.E.	1760.040	0.099	0.008	0.441	0.186	0.976	0.066	0.200
HR	σ_s^2	183.365	0.206	0.007	0.222	0.527	0.253	0.377	1.530
	S.E.	721.615	0.106	0.003	0.136	0.263	0.547	0.193	0.810
FL	σ_s^2	4431.405	0.443	0.000	0.000	0.402	0.228	0.039	1.835
	S.E.	2338.886	0.194	0.008	0.443	0.254	0.927	0.056	0.599
HR	σ_e^2	4821.160	0.388	0.010	0.512	0.925	4.189	0.561	3.242
	S.E.	986.994	0.085	0.002	0.115	0.210	0.722	0.139	0.740
FL	σ_e^2	5939.760	0.361	0.046	2.400	0.728	5.799	0.319	0.659
	S.E.	1618.810	0.114	0.010	0.528	0.202	1.225	0.073	0.286
HR	μ	1312.640	23.420	2.110	88.937	42.872	71.172	14.143	10.986
	S.E.	20.718	0.301	0.051	0.326	0.477	0.626	0.391	0.824
HR	μ	1204.610	26.757	2.912	85.493	46.501	70.291	11.720	12.422
	S.E.	50.153	0.442	0.084	0.603	0.517	0.942	0.255	0.782
HR	h^2	0.304	0.174	0.126	0.150	0.158	0.246	0.165	0.000
FL	h^2	0.415	0.244	0.288	0.051	0.324	0.000	0.074	0.072

¹DMY: dry matter yield; ADF: acid detergent fiber; ADL: acid detergent lignin; DMDig: digestible dry matter; NDF: neutral detergent fiber; NDFD: digestible NDF; Prot: protein; and WSC: water-soluble carbohydrate. σ_u^2 , σ_f^2 , σ_s^2 , and σ_e^2 are the genomic variance, variance due to uncorrelated family effects, spatial variance, and residual variance, respectively. S.E. is the asymptotic standard error and h^2 is the genomic heritability.